



## 1 Retrieval of aerosol properties from zenith sky radiance measurements

2 Sara Herrero-Anta<sup>1</sup>, Roberto Román<sup>1</sup>, David Mateos<sup>1</sup>, Ramiro González<sup>1</sup>, Juan Carlos  
3 Antuña-Sánchez<sup>2</sup>, Marcos Herreras-Giralda<sup>2</sup>, Antonio Fernando Almansa<sup>3,4</sup>, Daniel  
4 González-Fernández<sup>1</sup>, Celia Herrero del Barrio<sup>1</sup>, Carlos Toledano<sup>1</sup>, Victoria E. Cachorro<sup>1</sup>  
5 and Ángel M. de Frutos<sup>1</sup>.

6 <sup>1</sup>Group of Atmospheric Optics, University of Valladolid, Paseo de Belén 7, 47011 Valladolid, Spain.

7 <sup>2</sup>GRASP SAS, Remote Sensing Developments, Villeneuve D'Ascq, France

8 <sup>3</sup>Izaña Atmospheric Research Center (IARC), State Meteorological Agency of Spain (AEMET), 38001  
9 Santa Cruz de Tenerife, Spain.

10 <sup>4</sup>Cimel Electronique, 75011 Paris, France.

11 *Correspondence to:* Sara Herrero-Anta (sara@goa.uva.es)

12 **Abstract.** This study explores the potential to retrieve aerosol properties with the GRASP algorithm  
13 (Generalized Retrieval of Atmosphere and Surface Properties) using as input measurements of zenith sky  
14 radiance (ZSR), which are sky radiances measured in the zenith direction, recorded at four wavelengths by  
15 a ZEN-R52 radiometer. To this end, the ZSR measured at 440, 500, 675 and 870 nm by a ZEN-R52  
16 (ZSR<sub>ZEN</sub>), installed in Valladolid (Spain), is employed. This instrument is calibrated intercomparing the  
17 signal of each channel with coincident ZSR values simulated (ZSR<sub>SIM</sub>) at the same wavelengths with a  
18 radiative transfer model (RTM). These simulations are carried out using the GRASP forward module as  
19 RTM and the aerosol information from a collocated CE318 photometer belonging to the AERONET  
20 network (Aerosol and Robotic Network) as input. Dark signal and the signal dependence on temperature  
21 are characterized and included in the calibration process. The uncertainties on each channel are quantified  
22 by an intercomparison with a collocated CE318 photometer, obtaining lower values for shorter  
23 wavelengths; between 3% for 440 nm and 21% for 870 nm. The proposed inversion strategy for the aerosol  
24 retrieval using the ZSR<sub>ZEN</sub> measurements as input, so-called GRASP-ZEN, assumes the aerosol as an  
25 external mixture of five pre calculated aerosol types. A sensitivity analysis is conducted using synthetic  
26 ZSR<sub>ZEN</sub> measurements, pointing out that these measurements are sensitive to aerosol load and type. It also  
27 assesses that the retrieved aerosol optical depth (AOD) values in general overestimates the reference ones  
28 by 0.03, 0.02, 0.02 and 0.01 for 440, 500, 675, 870 nm, respectively. The calibrated ZSR<sub>ZEN</sub> measurements,  
29 recorded during two and half years at Valladolid, are inverted by GRASP-ZEN strategy to retrieve some  
30 aerosol properties like AOD. The retrieved AOD shows a high correlation with respect independent values  
31 obtained from the collocated AERONET CE318 photometer, with a determination coefficient ( $r^2$ ) about  
32 0.86, 0.85, 0.79 and 0.72 for 440, 500, 675 and 870 nm, respectively, and finding uncertainties between  
33 0.02 and 0.03 with respect to the AERONET values. Finally, it is studied the goodness of other retrieved  
34 aerosol properties like aerosol volume concentration for total, fine and coarse modes.

35 **Keywords:** zenith sky radiance, ZEN, GRASP, aerosol optical depth, AERONET, photometer

### 36 1. Introduction

37 Atmospheric aerosols constitute the biggest source of uncertainty in the assessment of Climate Change  
38 as assessed by Myhre et al., (2013), and yet, one decade later, not significant improvements have been made  
39 on this respect (Cissé et al., 2022). This is largely due to their high spatial and temporal variability across  
40 the globe and the complexity of its interaction with clouds (aerosol-cloud interactions) and solar radiation  
41 (aerosol-radiation interactions) (Boucher et al., 2013).

42 For a better understanding of aerosols and their behaviour and interactions, it is needed a high spatial  
43 and temporal monitoring coverage. Satellite measurements provides, in general, a high spatial resolution  
44 covering the whole Earth but with a low time resolution. On the other hand, some global ground-based  
45 networks, like AERONET (AERosol ROBOTIC NETwork; Holben et al., 1998), were established to monitor  
46 aerosols around the globe. In the case of AERONET, this network counts with hundreds of stations  
47 distributed worldwide and imposes standardization of instruments, calibration, processing and distribution.  
48 The standard instrument of AERONET is CE318 photometer (Cimel Electronique SAS), which records  
49 measurements of sun (and also lunar in recent models) irradiance and sky radiance in several wavelengths.  
50 Aerosol optical depth (AOD) can be derived using the measurements of sun (or lunar if available) such as



51 in the case of AERONET, applying the Beer-Lambert-Bouguer law on the instrument's output voltage as  
52 described in Holben et al. (1998) and Giles et al. (2019). AERONET also retrieves more complex aerosol  
53 properties, like aerosol size distribution and refractive indices, using an inversion algorithm that uses as  
54 input sky radiances at different angles and wavelengths, together with the AOD values (Sinyuk et al., 2020).

55 Another inversion algorithm is the GRASP code (Generalized Retrieval of Atmosphere and Surface  
56 Properties; [www.grasp-open.com](http://www.grasp-open.com)), which is a free and open-source code that allows a flexible retrieval of  
57 aerosol properties using measurements taken from many different instruments and a combination of them  
58 (Dubovik et al., 2014; 2021). The continuous development and versatility of the code allows to explore new  
59 alternatives to apply the code to different instruments. In this sense, some authors used GRASP to retrieve  
60 aerosol properties using as input measurements, among others, of: satellites (Chen et al., 2020; Wei et al.,  
61 2021); nephelometers (Espinosa et al., 2017); multi-wavelength AOD (Torres et al., 2017); AOD and sky  
62 radiance from photometers with signal from lidars (Lopatin et al., 2013; Benavent-Oltra et al., 2017; Tsekeri  
63 et al., 2017; Molero et al., 2020) or ceilometers (Román et al., 2018; Titos et al., 2019; Herreras et al.,  
64 2019); stand-alone all-sky cameras (Román et al., 2022) and their combination with lunar photometers  
65 (Román et al., 2017) and lidar (Benavent-Oltra et al., 2019).

66 A new instrument that could be used for GRASP retrievals is the ZEN-R52 (Sieltec Canarias S.L.),  
67 which has already been used to retrieve AOD values by other methods (Almansa et al., 2020). The ZEN-  
68 R52 measures the zenith sky radiances (ZSR) at five different wavelengths every minute, giving continuous  
69 ZSR values during daytime at 440, 500, 675, 870 and 940 nm (this latter channel is dedicated to the study  
70 of water vapour). As advantage, this instrument has not moving parts and, in general, is cheaper than more  
71 complex photometers, which allows the installation of more instruments obtaining a higher spatial  
72 coverage. Almansa et al., (2020) presented the ZEN-R52 and developed a method to retrieve AOD values  
73 from ZSR using a lookup table (LUT) created for the site of study, Izaña (Canary Island, Spain), considering  
74 uniquely dust aerosol, which is the main aerosol type in the area due to the proximity to the Saharan desert.

75 In this framework, the main objective of this work is to develop a new methodology to retrieve AOD  
76 and other aerosol properties with GRASP using calibrated ZSR at 440, 500, 675 and 870 nm from a ZEN-  
77 R52 instrument. This retrieval strategy is not linked to the place of study and therefore it allows to distribute  
78 the instrument worldwide, avoiding the need to create a different LUT for each site. In addition, we propose  
79 an in-situ method for the calibration of the ZEN-R52.

80 The following paper is structured as follows: Section 2 gathers information regarding the  
81 instrumentation and retrieval methods employed, as well as the study location. The procedure and results  
82 of the calibration of the ZSR at the four wavelengths used is explained in Section 3, while Section 4 is used  
83 to evaluate and drive a sensitivity study of the algorithm employed for the retrieval of aerosol properties.  
84 Finally, results obtained using the proposed methodology for the retrieval of aerosol properties are shown  
85 in Section 5, and Section 6 summarizes the main conclusions of the study.

86

## 87 2. Data and method

### 88 2.1 Site and instrumentation

#### 89 2.1.1 Valladolid GOA-UVa station

90 The place of study is located in Valladolid (Spain), a medium-sized city with a population of about 400000  
91 inhabitants including the metropolitan area. The city's climate is Mediterranean (Csb Köppen-Geiger  
92 climate classification). It presents predominantly 'clean continental' aerosol with frequent episodes of  
93 Saharan desert dust intrusions, especially in summer, when the highest AOD monthly mean values are  
94 reached (Bennouna et al., 2013; Román et al., 2014; Cachorro et al., 2016).

95 The Group of Atmospheric Optics of the University of Valladolid (GOA-UVa) manages an  
96 instrumentation platform installed on the rooftop of the Science Faculty (41.6636° N, 4.7058° W; 705 m  
97 asl), where diverse remote sensing instruments continuously run providing complementary information  
98 about radiance, clouds, water vapour, trace gases and aerosols. Two instruments from this station are used  
99 in this work: the CE318 photometer and the ZEN-R52 radiometer. The corresponding calculations and  
100 additional information will be referred and obtained for this location.

#### 101 2.1.2 CE318 photometers and AERONET products

102 Since 2006 the GOA-UVa has been one of the calibration facilities in charge of the calibration of  
103 AERONET standard instruments and is currently part of the European infrastructure ACTRIS (Aerosol,



104 Clouds and Trace Gases Research Infrastructure). The group is also actively contributing to the solar and  
105 moon photometry research (Barreto et al., 2019; González et al., 2020; Román et al., 2020). Due to  
106 calibration purposes, the GOA-UVA has almost always two reference AERONET photometers (masters)  
107 continuously operating on its rooftop platform for the calibration of the field instruments by  
108 intercomparison with these masters. The CE318 measures direct sun (and lunar for the recent model CE318-  
109 T; Barreto et al., 2016) irradiance at several narrow spectral bands by means of a rotating filters wheel.  
110 These direct measurements are used to derive the AOD (Giles et al., 2019) for all the available filters with  
111 ~~and~~ uncertainty of  $\pm 0.01$  for wavelengths longer than 440 nm and  $\pm 0.02$  for the UV (Holben et al., 1998).  
112 Sky radiances at several wavelengths are also measured by the CE318 on different scanning scenarios, and  
113 these sky radiances are combined with AOD values in the AERONET inversion algorithm to obtain  
114 microphysical and optical aerosol properties like aerosol volume size distribution and complex refractive  
115 index (Sinyuk et al., 2020). The sky radiances are calibrated against a calibrated integrating sphere  
116 following AERONET standards, obtaining an uncertainty of 5% for those measurements (Holben et al.,  
117 1998).  
118 In this work, we use AOD, sky radiance values and retrieved aerosol products from inversions from  
119 AERONET version 3 level 1.5. These data have been directly downloaded from the AERONET webpage  
120 (<https://aeronet.gsfc.nasa.gov>), which include near-real-time automatic cloud-screening and quality control  
121 filters (level 1.5). The inversion products with a sky error above 10% have been rejected in this study to  
122 warranty the quality of the retrievals.

### 123 2.1.3 ZEN-R52

124 The main instrument used in this work is the ZEN-R52 radiometer, installed in the GOA-UVA  
125 platform since April 2019. Since that moment the ZEN-R52 has been continuously operating in Valladolid,  
126 except for some short malfunction periods caused by technical issues. This study uses the recorded data  
127 from April 2019 until September 2021. The device was jointly developed by Sieltec Canarias S.L. and the  
128 Izaña Atmospheric Research Center (IARC) to monitor AOD from sky radiance measurements at the zenith  
129 direction and at different spectral bands (Almansa et al., 2017; 2020). The instrument has five filters with  
130 nominal wavelengths centred at 440, 500, 675, 870 and 940 nm with a bandwidth of 10 nm and an estimated  
131 precision of  $\pm 2$  nm in the central wavelength. Each filter is over a silicon diode (350–1050 nm) with a 16-  
132 bit resolution, over a high dynamic acquisition range. The 940 nm filter was recently included in this new  
133 version for precipitable water vapour retrieval but this channel is not used in this work since it is focused  
134 on aerosols. The ZEN-R52 optical configuration achieves a field of view smaller than  $2^\circ$ . It is equipped  
135 with a small aluminium weatherproof and protected by a thick borosilicate BK7 window, with no moving  
136 parts. All of this is mounted in such a way that the collimated sky radiance in the direction of the zenith  
137 reaches to the sensors. The instrument results to be very robust and can operate in a wide temperature range,  
138 between  $-40^\circ$  and  $85^\circ\text{C}$ . A more detailed technical description of the instrument can be found in Almansa  
139 et al. (2017; 2020).

140 The zenith sky radiance measurements at all channels are made simultaneously, providing an  
141 output signal in analogic-to-digital units (ADU) every minute. This output is the computed average of 30  
142 samples taken within the minute, providing also an error (ZEN error) associated to the measurement which  
143 is the standard deviation of the 30 samples.

### 144 2.2 GRASP methodology

145 GRASP contains mainly two independent modules: the ‘forward model’ and the ‘numerical  
146 inversion’. The first one is a radiative transfer model (RTM) used to simulate atmospheric remote sensing  
147 observations for a characterized atmosphere. The second module, based on the multi-term least squares  
148 method (Dubovik and King, 2000), is used in combination with the RTM for a statistically optimized fitting  
149 of the observations to retrieve aerosol properties from radiometric measurements (Dubovik et al., 2014).  
150 This provides the algorithm with high flexibility since different constrains can be applied to the retrieval  
151 and can be modified in order to adapt the retrieval to each specific situation. It is important to mention that  
152 GRASP works with normalized radiances ( $I_{GRASP}$ ), which are related with the measured radiances as:

$$153 I_{GRASP} = I_{meas} * \pi/E_0 \quad (1)$$

154 Where  $I_{meas}$  is the radiance measured by the instrument and  $E_0$  is the extraterrestrial solar  
155 irradiance, both expressed in the same units. The standard ASTM-E490 solar spectrum has been used in  
156 this work for the normalization of Eq. (1). This spectrum was calculated for moderate solar activity and



157 medium Sun-Earth distance; therefore, it has been corrected from Sun-Earth distance for each day of the  
158 year.

#### 159 2.2.1. Forward module

160 The GRASP forward module is a RTM based on the Successive Orders of Scattering approach  
161 (Lenoble et al., 2007; Herreras-Giralda et al., 2022) which requires information about aerosol, gas, site  
162 coordinates and date-time together with the solar zenith angle (SZA) to characterize the atmosphere  
163 scenario. In this study gases and aerosol information are extracted from AERONET direct and inversion  
164 products available at Valladolid station. For the gases it has been used the gases optical depth (GOD), while  
165 the used aerosol information has been size distribution (in 22 log spaced bins of radius), sphere fraction and  
166 complex refractive indices at 440, 675 and 870 nm. Complex refractive index at 500 nm has been  
167 interpolated from the values at 440 and 675 nm. The bidirectional reflectance distribution function (BRDF)  
168 data is also used as input in GRASP. The used BRDF values are extracted from an 8-day climatology  
169 created for the place of study using satellite data; specifically, the MCD43C1 product from MODIS V005  
170 collection (Schaaf et al., 2011) for the 2000–2014 period (see Román et al. 2018 for more details about  
171 these climatology values).

172 The ZSR has been simulated at 440, 500, 675 and 870 nm with the GRASP forward module using  
173 all the mentioned input data whenever it was available. These simulations have been used for calibration  
174 purposes as can be observed in Section 3, but also for the sensitivity analysis with synthetic data of Section  
175 4.2. ZSR simulations are also performed for Section 4.1, but in this case the aerosol properties have been  
176 obtained for precalculated aerosol types instead of real data from AERONET.

#### 177 2.2.2 Inversion strategy

178 The present study aims to retrieve aerosol properties with GRASP using as input the calibrated  
179 ZSR from the ZEN-R52 at four effective wavelengths. The versatility of GRASP allows different  
180 approaches to model aerosols to maximize the possibilities of the different retrieval schemes. Due to the  
181 reduced amount of information produced by the ZEN-R52, the approach called ‘models’ has been chosen  
182 (Chen et al., 2020). This is a simple and fast processing approach where aerosol is assumed to be an external  
183 mixture of several aerosol models. In this case the approach assumes five aerosol types which correspond  
184 to the typical aerosols on Earth: smoke, urban, oceanic, dust and urban polluted. Each model has a fixed  
185 particle size distribution, refractive indices and sphere fraction, containing the already pre-calculated phase  
186 matrix, and the extinction and absorption cross-sections (see Fig. S1 for a representation of the size  
187 distribution of each model).

188 This way, the inversion strategy retrieves only five independent parameters: the total aerosol volume  
189 concentration and the fraction of four models in the mixture (the fifth fraction equals one minus the rest of  
190 the fractions). All these retrieved parameters allow to obtain other complex aerosol properties, like size  
191 distribution parameters, weighting the individual properties of each model, which are known, by their  
192 fraction of the mixture. The size distribution parameters that can be obtained are volume median radius of  
193 fine (RF) and coarse (RC) modes, standard deviation of lognormal distribution for fine ( $\sigma_F$ ) and coarse  
194 ( $\sigma_C$ ) modes, and aerosol volume concentration for fine (VCF) and coarse (VCC) modes and the total value  
195 (VCT). AOD can be also calculated and it is given for each wavelength directly in the GRASP output. Each  
196 output, one per retrieval, provides the relative residual differences between the measured ZSR (input) and  
197 the ones generated after the inversion (simulated by GRASP forward module under the retrieved scenario)  
198 for each wavelength. This residual information will be used to evaluate the goodness of the retrievals,  
199 rejecting the non-convergent ones.

200 This proposed strategy requires as input: the calibrated ZSR at four wavelengths, the coordinates  
201 of the site, date, time, SZA, the BRDF values obtained from the climatology mentioned above, and the  
202 GOD at each wavelength to account for gases effect. The GOD used in this work is obtained from a monthly  
203 GOD climatology, which has been created using GOD data retrieved from AERONET for the 2012-2021  
204 period in Valladolid. This proposed inversion strategy to retrieve aerosol properties with GRASP using  
205 ZEN-R52 measurements has been named as ‘GRASP-ZEN’.

206

### 207 3. Calibration



208 A methodology for the ZEN-R52 calibration is proposed in this Section. This methodology is a field  
209 campaign which does not require laboratory measurements except for the dark signal characterization, and  
210 it is based on four steps: dark signal correction, quality data filtering, temperature correction, and a final  
211 comparison against simulated values to convert the output signal from ADU into radiance units ( $\text{Wm}^{-2}\text{nm}^{-1}\text{sr}^{-1}$ ).  
212 With this purpose ZSR simulations have been performed for the whole dataset of ZEN-R52  
213 measurements, using the GRASP forward module fed with the closest AERONET information (Section  
214 2.2.1) whenever it was available within  $\pm 5$  minutes from the ZEN-R52 measurement; considering in good  
215 approximation, and as checked later, that aerosol conditions will not change significantly within 5 minutes.  
216 Only those AERONET retrievals with a sky error lower than 5% have been used to ensure the quality of  
217 the simulations, obtaining a total of 4725 data pairs.

218  
219

### 3.1. Dark signal correction

220 For the dark signal (DS) evaluation, the instrument was fully covered with a black piece and  
221 introduced into a thermal chamber in the GOA-UVa facilities. The instrument was subjected to a  
222 temperature variation in the range from  $-10$  to  $50$  °C in darkness conditions. The dark signal registered by  
223 each channel at each temperature is shown in Figure 1. It shows a constant behaviour for 440 and 500 nm  
224 filters. Contrary, for the other wavelengths a stepped exponential behaviour can be seen. In order to  
225 characterize this behaviour, the logarithm of the ZEN dark signal has been fitted to a three-degree  
226 polynomial. This fitting is after rounded up to the unit to obtain a stepped fitting. The modelled dark signal  
227 is also represented in Figure 1 by the black lines. This modelling has been used to subtract the corresponding  
228 dark signal value to the raw signal, obtaining dark signal corrected ZSR ( $\text{ZSR}_{\text{DSC}}$ ). The DS signal has been  
229 characterized in the laboratory in this work in order to cover a high range of temperatures, but it could be  
230 calculated from the night-time measurements (dark sky) when a thermal chamber is no available.

231

### 3.2 Quality control filtering criteria

232 With the dark signal corrected, we compare the field measurements of  $\text{ZSR}_{\text{DSC}}$  against the ZSR  
233 simulated values ( $\text{ZSR}_{\text{SIM}}$ ). This comparison is shown in Figure 2. The points colour in the scatter plots of  
234 Figure 2 represent the density of points per pixel as defined by Eilers and Goeman (2004), using a  $\lambda=50$  for  
235 smoothness; all the density scatter plots of this paper were done with the same configuration. The  
236 determination coefficient ( $r^2$ ) is also added in the panels of Figure 2, showing in general good agreement  
237 for each channel between  $\text{ZSR}_{\text{DSC}}$  and  $\text{ZSR}_{\text{SIM}}$  but with some outliers regarding the linear trend (see left  
238 panels a, c, e and g). These outliers present higher  $\text{ZSR}_{\text{DSC}}$  values than expected and they could be caused  
239 by the presence of clouds in the zenith, instrument malfunction and others.

240 To identify and reject the cloud-contaminated or wrong measurements, several parameters have  
241 been considered in this subsection: SZA, ZEN error, temperature, and the time interval between the  
242 inversion used to simulate the  $\text{ZSR}_{\text{SIM}}$  and the corresponding  $\text{ZSR}_{\text{DSC}}$ . Some thresholds have been identified  
243 after the visual analysis of these parameters in the scatter plot. For the SZA, the signal of ZEN instrument  
244 is higher than the expected for SZA values below  $30^\circ$ , which could be explained by some stray sun light  
245 coming to the sensors due to the high elevation of the Sun. Then,  $\text{ZSR}_{\text{DSC}}$  values recorded under SZA below  
246  $30^\circ$  have been discarded, but also the values with SZA above  $80^\circ$  due to the low signal registered for this  
247 SZAs (See Figure S2 for a clear overview). The ZEN error parameter (Section 2.1.3) can be assumed as a  
248 cloud presence indicator, since measurements affected by clouds should register a high ZEN error due to  
249 the high variability of the sky radiances during the 1-min measurement. An evaluation of Figure 2 but with  
250 points classified by its ZEN error at 440 nm led us to establish a threshold of 4% for the ZEN error in the  
251 four channels (See Figure S3). If the measurement of any channel has a ZEN error above this threshold,  
252 then the measurements of the four channels are rejected.

253 No clear dependence of the outliers on the rest of the parameters has been observed. The results  
254 after applying the mentioned filters ( $30^\circ < \text{SZA} < 80^\circ$ ; ZEN error  $< 4\%$ ) are represented in the right panels  
255 (b, d, f and h) of Figure 2. The number of coincident measurements is reduced to 4369 points after applying  
256 the quality control but a significant improvement in the determination coefficients is observed, rising from  
257 0.96 to 0.99 for the 440nm channel and from 0.80 to 0.95 in the case of 870nm. From now on, all the  
258  $\text{ZSR}_{\text{DSC}}$  measurements used will be assumed to satisfy this quality control unless specified.

259

### 3.3 Temperature correction



260 In order to check the dependence with temperature of each filter the ratio  $ZSR_{DSC}/ZSR_{SIM}$   
261 normalized by the mean ratio is plotted against the temperature in Figure 3. In the left panels (a, c, e and g)  
262 of Figure 3 all data points are represented together with the linear fit, showing a constant behaviour for 440  
263 and 500 nm, but a clear trend for 675 and 870 nm channels. In order to despise outliers, the ratios were  
264 grouped by 2°C bins and its median was calculated whenever the group had at least 40 points. These median  
265 values are plotted against the mean temperature of the group's temperatures in Figure 3 right panels (b, d,  
266 f and h). The corresponding linear fit coefficients obtained in Figures 3f and 3h has been established to be  
267 used to correct the  $ZSR_{DSC}$  at 675 and 870 nm applying the next Equation 2:

$$268 \quad ZSR_{TC}(\lambda) = \frac{y_{20}(\lambda)}{a(\lambda)+b(\lambda)T} ZSR_{DSC}(\lambda); \lambda = 675, 870\text{nm} \quad (2)$$

269 where  $ZSR_{DSC}$  is the ZEN signal after dark signal correction and  $ZSR_{TC}$  is this signal with the  
270 temperature correction; a and b represent the intercept and slope of the final linear fits, respectively;  $y_{20}$  is  
271 the correspondent y-axis value of the linear fit at the temperature T of 20° C (arbitrary value chosen to  
272 normalize). This temperature correction is only applied to the  $\lambda$ -wavelengths of 675 and 870 nm.

### 273 3.4. Calibration coefficients

274 Once the dark signal correction, quality filtering and temperature correction are applied to the  
275 ZEN-R52 raw signal, the definitive comparison between the ZSR from the ZEN-R52 and the ZSR values  
276 simulated by GRASP forward module can be done to obtain the calibration coefficients. The density scatter  
277 plots between  $ZSR_{SIM}$  values and  $ZSR_{TC}$  are shown in Figure 4. The slope of the linear fit directly represents  
278 the calibration coefficients obtained to transform the  $ZSR_{TC}$  signal into radiance units ( $Wm^{-2}nm^{-1}sr^{-1}$ ) for  
279 each channel. This calibrated radiance is named  $ZSR_{ZEN}$  hereafter.

280 The obtained calibration coefficients and the ones obtained by intercomparison with a calibrated  
281 integrating sphere at IARC facilities are shown in Table 1. Table 1 also presents the relative differences  
282 between both calibration coefficients using the coefficients from IARC as reference; the uncertainty  
283 involved in the latter calibration method procedure is estimated to be 5% by Walker et al. (1991) These  
284 differences are 1.39%, -6.54%, -6.72% and -5.89% for 440, 500, 675 and 870 nm, respectively. The  
285 proposed calibration method uses the standard ASTM-E490 solar spectrum for transforming the unitless  
286 output from GRASP, as indicated in Equation 1. This fact can increase the relative differences between the  
287 two calibration methods. However, the calibration method employed here allows to use the same  
288 normalization factor that lately will be applied to the  $ZSR_{ZEN}$  measurements that will be introduced in the  
289 GRASP inversion module, avoiding to introduce a systematic error due to the normalization required by  
290 the algorithm. It means that this calibration method is better suited when using the  $ZSR_{ZEN}$  values as input  
291 for GRASP to retrieve aerosol properties, since there is no need for extraterrestrial spectrum normalization.  
292 From now on  $ZSR_{ZEN}$  will stand for the calibrated zenith sky radiances measured by the ZEN-R52 satisfying  
293 the established quality controls ( $30^\circ < SZA < 80^\circ$ ; ZEN error < 4%).

### 294 3.5. ZEN-R52 vs. CE318 photometer comparison

295 In order to check the goodness of the calibrated ZEN-R52 measurements, the  $ZSR_{ZEN}$  observations  
296 have been compared with measurements recorded by collocated CE318 instruments for the ~~hole~~ available  
297 dataset of ZEN-R52 measurements. For the comparison, independent measurements from CE318  
298 photometers for two different scenarios are employed: the cloud mode (CM) and the principal plane  
299 scanning (PPL).

#### 300 3.5.1. Cloud Mode

301 The CE318 sun-sky photometer allows to perform measurements in the 'cloud mode' scenario. It  
302 is carried out when the direct sun measurement indicates an obscured sun, and therefore the aerosol retrieval  
303 is not possible. This scenario orientates the sensor head into the zenith direction and takes zenith radiance  
304 measurements at 9 s intervals for each wavelength, which are obtained by successively rotating an  
305 interference filter in front of the detector. The 'cloud mode' scenario was originally implemented to obtain,  
306 during this idle time, cloud optical depth from zenith sky radiances at the spectral wavelengths employed  
307 by the sun-sky photometer (Chiu et al., 2010) as suggested by Marshak et al., (2000) and Barker and  
308 Marshak, (2001).



309 The zenith sky radiances measured under the cloud mode ( $ZSR_{CM}$ ) have been directly downloaded  
310 from the AERONET network webpage. For the comparison with ZEN-R52, quasi-coincident (the closest  
311 within  $\pm 1$  min)  $ZSR_{ZEN}$  and  $ZSR_{CM}$  measurements have been obtained and plotted in Figure 5, showing a  
312 good correlation between both datasets. The deviation between them is high, likely due to the short-time  
313 variation in the cloud radiative field. Figure 5 includes all the  $ZSR_{ZEN}$  measurements; the filtering to SZA  
314 values and ZEN errors is not applied, since the cloud mode measurements is under cloud presence. In this  
315 case, there is not dependence on SZA; outliers do not appear for  $SZA < 30^\circ$  values. Hence, the  $ZSR_{ZEN}$  values  
316 are only wrong for  $SZA < 30^\circ$  when the sun is cloud-free, which confirms the suggested explanation that  
317  $ZSR_{ZEN}$  measurements are contaminated by stray sun light under cloud-free conditions when the sun  
318 elevation is high ( $SZA < 30^\circ$ ). In addition, it was checked that 86% of the ZEN-52 measurements used in  
319 this comparison (which are known to be affected by clouds), present a ZEN error  $> 4\%$  at least for one  
320 channel. This also validates the proposed use of the ZEN error as a rough ‘cloud screening’.

### 321 3.5.2. Principal plane scan

322 CE318 sun-sky photometers allow to perform three different scanning scenarios for sky radiance  
323 measurements. One of these scanning scenarios is in the principal plane (PPL) geometry, where the azimuth  
324 angle is equal to the solar azimuth angle while the zenith angle varies measuring sky radiances at the same  
325 fixed angles regards the SZA. This is done sequentially once for each channel starting at 870nm, followed  
326 by 675, 500 and 440 nm channels for each PPL scenario. The PPL geometry allows to extract the ZSR by  
327 linear interpolation of the PPL points to the zenith position. In this situation, the cloud screening of PPL  
328 points has been made checking the smoothness of the PPL curve as described in Holben et al. (1998). The  
329 smoothness criterion analyses the second derivative of the PPL radiances with respect to the scattering  
330 angle. This way the PPL measurement is classified as cloud contaminated if the second derivative is  
331 negative (the threshold is not 0 but  $-1 \times 10^{-7}$  as empirically determined) at any scattering angle between 2  
332 and  $90^\circ$  (Almansa et al., 2020) The obtained ZSR from this method, based on the interpolation of cloud-  
333 screened CE318 sky radiances measured in the PPL geometry, has been labelled as  $ZSR_{PPL}$ .

334 The PPL dataset is not directly available in the AERONET webpage; then, it has been extracted  
335 from CAELIS database (Fuertes et al., 2018; González et al., 2020).  $ZSR_{ZEN}$  and  $ZSR_{PPL}$  measurements  
336 within  $\pm 1$  min, are compared in Figure 6. Upper panels (a-d) of Figure 6 show the density scatter plots of  
337  $ZSR_{ZEN}$  against the reference  $ZSR_{PPL}$ , where a high correlation between both datasets can be observed for  
338 all the channels, varying the determination coefficients from 0.94 at 870 nm to 0.99 at 440 and 500 nm. In  
339 general, the number of outliers is higher for longer wavelengths.  
340 In order to evaluate the uncertainty of the  $ZSR_{ZEN}$  measurements using  $ZSR_{PPL}$  as reference, the relative  
341 differences between  $ZSR_{ZEN}$  and  $ZSR_{PPL}$  ( $\Delta ZSR_{ZEN-PPL}$ ) have been evaluated and represented in frequency  
342 histograms in the bottom panels (e-h) of Figure 6. These panels also include the mean (mean bias error;  
343 MBE), median (Md) and standard deviation (SD) of  $\Delta ZSR_{ZEN-PPL}$ . The median values, less sensitive to  
344 outliers, are close to zero (Md = 1.36%, -1.39% and -0.22% for 440, 500 and 675 nm, respectively)  
345 indicating that the  $ZSR_{ZEN}$  are accurate regarding the reference  $ZSR_{PPL}$  values, except for 870 nm channel  
346 which Md value of 4.99% points out an overestimation of the reference ZSR values. Nevertheless, the  
347 precision decreases for longer wavelength channels, from SD values of 3.00% and 4.62% for 440 and 500  
348 nm, respectively, to SD=12.54% and 21.37% for 675 and 870 nm.

349 All these statistical parameters have been calculated also considering the calibration coefficients,  
350 without temperature correction, obtained at IARC with a calibrated integrating sphere. These parameters,  
351 and the previously obtained by the proposed method of this work, are shown in Table 2 in order to observe  
352 which calibration provide ZSR values closer to the reference  $ZSR_{PPL}$  values. The results of Table 2 show  
353 that the ZSR obtained with the proposed calibration method, based on intercomparison with ZSR  
354 simulations, is in general more accurate and precise except for 440 nm. Although the results of Table 2 for  
355 440 nm are worse for the proposed calibration than for IARC calibration, the results are still good for the  
356 proposed method with MBE close to 0 and a low value of SD. The  $ZSR_{ZEN}$  values from IARC calibration  
357 are not temperature corrected, which could be behind of part of the observed differences.

358 All these results indicate that the  $ZSR_{ZEN}$  at 440 and 500 nm values are more accurate and precise than  
359 at 675 and 870 nm. Then,  $ZSR_{ZEN}$  measurements at shorter wavelengths should have more weight in the  
360 aerosol retrieval than the measured for longer ones, since measurements at 440 nm and 500 nm are more  
361 trustable. The inversion module from GRASP code takes into account the weight of each measurement  
362 through the so-called ‘noises’; allowing to associate a different noise to each channel in this case. Therefore,



363 the obtained standard deviation of Table 2 (using the calibration proposed in this work), associated with the  
364 ZSR<sub>ZEN</sub> uncertainty, will be introduced for each channel in GRASP for the GRASP-ZEN method to account  
365 for the different reliability of each channel.

#### 366 4. Sensitivity analysis

367 In order to analyse the capabilities of the proposed inversion strategy to invert ZSR<sub>ZEN</sub> measurements  
368 with GRASP, a detailed sensitivity analysis is carried out in this section using synthetic data.

369 As mentioned in Section 2.2.2, the chosen method to obtain aerosols properties, considers five aerosol  
370 types or ‘models’, which have fixed size distribution, refractive indices and sphere fraction. The method  
371 must retrieve aerosol properties from measurements of ZSR<sub>ZEN</sub> at 440, 500, 675 and 870nm. Sky radiances  
372 depend on aerosol concentration and type, among other factors like the scattering angle and SZA; hence  
373 they are commonly used to retrieve aerosol properties by measuring them at different scattering angles and  
374 wavelengths (Nakajima et al., 1996; Román et al., 2022). Figure S4 shows in the supplementary material  
375 the sky radiances in the zenith direction, modelled by GRASP for different aerosol concentrations, and how  
376 they are sensitive to changes in the AOD and aerosol type for the five aerosol types used by the inversion  
377 method. This figure shows that for higher SZA (Figure S4; panels i-l) the ZSR values are less sensitive to  
378 aerosol type and concentration, since different scenarios show smaller differences in the corresponding  
379 ZSR. Nevertheless, lower SZA conditions (Figure S4; panels a-d) show a clear sensitivity to type and  
380 aerosol load for AOD at 440nm below 0.7, that would represent an extreme AOD event (Mateos et al.,  
381 2020).

382 To explore the limitations of the retrieval of aerosol properties following the proposed inversion  
383 strategy, two different tests have been carried out. For both tests, artificial aerosol scenarios have been  
384 created and used as input to the GRASP forward module to simulate the ZSR that the ZEN-R52 would  
385 register under these synthetic scenarios (ZSR<sub>SYN</sub>). Since the ZSR<sub>SYN</sub> values are artificially created, they will  
386 be randomly perturbed following a Gaussian distribution defined by the uncertainty of each channel  
387 previously calculated for the ZEN-R52 in order to create realistic observations (similar to Torres et al.,  
388 2017 and Román et al., 2022, among others). The perturbed ZSR<sub>SYN</sub> will be then used as input in the  
389 inversion module, following the GRASP-ZEN method. It will provide the retrieved aerosol properties as  
390 output, which will be labelled with the subindex ‘INV’ referring to ‘inversion’. The test is focused on the  
391 capability to retrieve AOD values and size distribution properties.

#### 392 4.1. Scenarios from the combination of five aerosol types

393 This test creates random synthetic aerosol scenarios formed by a mixture of the five aerosol types  
394 used by the ‘models’ GRASP inversion strategy (see Section 2.2.2). We aim here to assess the capabilities  
395 of the retrieval of aerosol properties if the observed aerosol is actually a pure mixture of these five types of  
396 aerosol. To this end, random fractions of each aerosol type are selected together with a random aerosol  
397 concentration chosen in the interval from 0.01 to 0.15  $\mu\text{m}^3/\mu\text{m}^2$  creating a total of 1000 scenarios. The  
398 simulations have been made for three different SZA values (30, 50 and 70°), but we will focus here in the  
399 SZA=50° situation, which would represent a half-way and common scenario for the latitude of Valladolid.

400 Figure 7 shows the retrieved AOD (AOD<sub>INV</sub>), using as input the perturbed ZSR<sub>ZEN</sub> of each  
401 created random scenario for SZA equal to 50°, against its original synthetic AOD value (AOD<sub>SYN</sub>). The  
402 same graphs for SZA values of 30° and 70° are shown in the Figure S5 of the supplementary material. In  
403 general, the data deviation increases for high AOD values, which are less frequent. For SZA equal to 50°,  
404 the method overestimates the aerosol load for all the wavelengths, with MBE ranging from 0.23 to 0.11.  
405 The best results are obtained for SZA = 30°, with absolute mean bias errors lower than 0.002 for all  
406 wavelengths and the lowest uncertainty (standard deviation lower than 0.66); while for SZA = 70° the  
407 method slightly underestimates the AOD with MBEs ranging from -0.004 to 0. It is important to point out  
408 that the convergence capability of the method decreases for high SZA, being the convergent inversions a  
409 total of 43.2% and 43.6% at SZA=30° and 50° respectively but only 27.1% for SZA=70°; considering that  
410 there are initially 1000 scenarios. These results could be related to the dependence of the ZSR sensitivity  
411 on the SZA, which is higher for lower SZA, and therefore would make easier for the method to find a  
412 solution.

413 For the size distribution the frequency histograms of the absolute differences between the inverted  
414 and the synthetic parameters are shown in Figure 8 to have a clear overview of the results obtained (a direct  
415 scatter plot comparison is shown in Figure S6). For the current synthetic test, the retrieval of size





416 distribution properties is very accurate and precise, showing Md values very close to zero for all the  
417 properties. For the volume median radius the precision is high with  $SD < 10\%$  for both fine and coarse  
418 modes, but the precision is worse for the aerosol volume concentration with an SD value about 33.2% for  
419 the total concentration. These results could be explained, at least in part, due to the fixed size distributions  
420 for the ‘models’, which present similar RF, RC,  $\sigma_F$  and  $\sigma_C$  values and, therefore, it will not show an  
421 important variation when combining them, but contrary, the aerosol volume concentration is an extensive  
422 property and therefore can have a higher variation.

#### 423 4.2. AERONET scenarios

424 The same procedure than in the previous test is developed in this one but using realistic aerosol  
425 properties retrieved at Valladolid by AERONET. For this new test, all the available inversions (almucantar  
426 and hybrid scans) from AERONET for the coincident ZEN-R52 measurement period (2019-2021) with and  
427 sky error  $< 5\%$  have been obtained, achieving a total of 5321 synthetic scenarios. With this test we aim to  
428 assess the capabilities of the method to retrieve the aerosol properties when the ZSR come from an aerosol  
429 scenario closer to real aerosol conditions and not necessarily to a mixture of the five mentioned aerosol  
430 types. In this situation the  $ZSR_{SYN}$  simulations are made for the corresponding date and time at which the  
431 AERONET inversion product was retrieved, achieving a wide variety of SZA values ( $18^\circ < SZA < 78^\circ$ ).

432 Figure 9 presents the comparison between the  $AOD_{INV}$ , obtained from the inversion of the  
433 perturbed  $ZSR_{SYN}$  as input in GRASP-ZEN method, and  $AOD_{SYN}$  for these AERONET synthetic scenarios.  
434 This comparison reveals a clear overestimation of the inverted AOD values compared to the original ones  
435 for the four wavelengths, ranging the MBE values from 0.01 to 0.04 and the Md from 0.01 to 0.03 for the  
436 differences between both datasets. These results could be related with the previous results for overestimated  
437 AOD at  $SZA = 50^\circ$ , but in this situation the overestimation is not related to the SZA since it has been  
438 checked that points with different SZA are homogeneously distributed, therefore  $AOD_{SYN}$  is always  
439 overestimated by the obtained from GRASP-ZEN for all SZA. The standard deviation of the AOD  
440 differences, which can be associated with the uncertainty in  $AOD_{INV}$ , is above 0.02, being 0.05 for 440 and  
441 500 nm, which are higher than the standard deviation obtained in the previous section for all wavelengths  
442 and SZAs,  $SD = 0.090$  (for AOD 440 nm at  $SZA=50^\circ$ ).

443 The reason for the observed overestimation could be in the limitations of the GRASP-ZEN method  
444 based on the ‘models’ approach, which only allows to retrieve aerosol properties within the properties of  
445 the five aerosol types. It means that, for example, if the real aerosol has a median radius of fine mode bigger  
446 than the ones of the five ‘models’, then the GRASP-ZEN retrieval will underestimate the real median radius  
447 of fine mode and this difference will be compensated unbalancing other aerosol properties to fit the  
448 measured ZSR and the synthetic ZSR values of the retrieved aerosol scenario (to reduce the residual  
449 differences in ZSR values).

450 To explore this hypothesis, the retrieved size distribution properties have been compared with the  
451 synthetic ones. The frequency histograms for the absolute differences between the inverted and the  
452 synthetic properties are shown in Figure 10 (the direct scatter plot comparison can be seen in Figure S7).  
453 The retrieved volume concentrations present median differences regarding the synthetic ones about  
454  $0.01 \mu\text{m}^3/\mu\text{m}^2$  for VCF and VCT, while this median value is close to zero for the VCC. The retrieved fine  
455 intensive properties underestimate the reference values, being the median values of their differences about  
456 -14% and -10% for RF and  $\sigma_F$ , respectively, and -10% and -4% for RC and  $\sigma_C$ , respectively.

457 This lack of accuracy is the main difference between the results of Figure 10 and Figure 8. As  
458 mentioned before, we would expect a big accuracy and precision in the retrieved values of the volume  
459 median radius and standard deviation for the ‘models’ combination scenarios test (Section 4.1), since the  
460 scenario can be perfectly reproduced by GRASP-ZEN because it is a combination of the same models used  
461 in the inversion module; however, for a real aerosol scenario (the test for AERONET scenarios of this  
462 subsection), these properties could be impossible to obtain with enough accuracy since they present wider  
463 range of size distributions than the offered by the ‘models’ approach. Similar results are expected for the  
464 real and imaginary refractive index and other optical properties, due to the limitations of the ‘models’  
465 approach.

466 The results of this section conclude that the GRASP-ZEN method is useful for the retrieval of  
467 AOD but nor for some size distribution properties, like the volume median radius and standard deviation



468 of fine and coarse modes. Therefore, we will focus on the retrieval of AOD at 440, 500, 675 and 870 nm  
469 and VCF, VCC and VCT.

## 470 5. Results

471 Once the  $ZSR_{ZEN}$  measurements have been obtained from ZEN-R52 by the calibration method  
472 proposed in Section 3, and the GRASP-ZEN method has been proved in Section 4 as capable to retrieve  
473 some aerosol properties like AOD, the GRASP-ZEN methodology has been applied to all the available  
474 dataset from ZEN-R52 measurements at Valladolid, obtaining a total of 222663 GRASP-ZEN retrievals.  
475 This dataset has been obtained using  $ZSR_{ZEN}$  measurements which satisfy the filtering criteria, regarding  
476 SZA and ZEN error, determined in Section 3.2. The retrievals which do not present enough convergence  
477 have been removed, which led to a total of 170637 retrievals. This convergence check is based on the  
478 residuals of the inversion process (see Section 2.2.2). A cloud-screening filter is applied, based mainly on  
479 the retrieved AOD at 500 nm, following a similar procedure as Giles et al. (2019) for cloud-screening in  
480 AERONET version 3. Three checks are applied for this cloud-screening: smoothness, stand-alone and  $\pm 3\sigma$ .  
481 The smoothness check is done by the analysis of the AOD variation at 500 nm: for each two subsequent  
482 values if the variation is higher than 0.01/min the retrieval with larger AOD at 500 nm in the pair is removed.  
483 After the smoothness, the stand-alone check is applied: all single retrievals remaining which are more than  
484 1 hour apart from the closest available retrieval are removed. Finally, for each day the daily mean and  
485 standard deviation are calculated for the retrieved AOD at 500 nm and for the Ångström Exponent (AE;  
486 Ångström, 1964) obtained with the four retrieved AOD values (440, 500, 676 and 870 nm). To satisfy the  
487  $\pm 3\sigma$  check, the retrieved AOD at 500 nm and AE must be within the daily mean  $\pm 3\sigma$  (triple standard  
488 deviation). Values not satisfying this requirement are removed. A final dataset with 126112 points  
489 satisfying the convergence and cloud-screening criteria is obtained.

### 490 5.1 Aerosol Optical Depth

491 The AOD retrieved by GRASP-ZEN using the  $ZSR_{ZEN}$  measurements ( $AOD_{GRASP\_ZEN}$ ) has been  
492 compared against independent AOD measurements from AERONET ( $AOD_{AERONET}$ ) derived from CE318  
493 sun-sky photometers collocated with the ZEN-R52 at Valladolid. Figure 11 shows the complete time series  
494 evolution of  $AOD_{GRASP\_ZEN}$  together with  $AOD_{AERONET}$ , both at 440 nm. Despite some  $AOD_{GRASP\_ZEN}$   
495 outbreaks which are not reproduced by the  $AOD_{AERONET}$ , both datasets show in general a similar temporal  
496 evolution. Figure 12 shows a more detailed view of these data in a shorter period, from 16 to 22 June 2020,  
497 with high availability of data from both GRASP-ZEN and AERONET datasets for the four available  
498 wavelengths. A lack of AOD values in the GRASP-ZEN dataset around mid-day is observed; it is explained  
499 by the rejection of ZEN-R52 measurements for SZA below  $30^\circ$ , which, in the analysed period and latitude,  
500 occurs around mid-day. In Figure 12 (panels a–d) it can be also observed that both GRASP-ZEN and  
501 AERONET datasets vary with time in a similar way for all the wavelengths, with AOD values from  
502 GRASP-ZEN slightly overestimating the AOD values from AERONET at all wavelengths. Figure 12 (panel  
503 e) includes the  $AOD_{GRASP\_ZEN}$  at 440, 500, 675 and 870 nm in the same plot, showing the behaviour  
504 expected for the AOD at these wavelengths: AOD decreasing with wavelength and parallel time evolution.

505 To perform a more quantitative analysis of the correlation between these datasets, a match-up of  
506 AERONET AOD ( $AOD_{AERONET}$ ) data with GRASP-ZEN AOD ( $AOD_{GRASP\_ZEN}$ ) values within 1.5 minutes  
507 has been made, obtaining a total of 37787 coincident points per wavelength. The AOD data from GRASP-  
508 ZEN is represented against the coincident AOD from AERONET in a density plot in Figure 13 for each  
509 wavelength (panels a–d). This figure (panels e–h) also shows in the bottom panels the frequency histograms  
510 of the differences between both AOD datasets.  $AOD_{GRASP\_ZEN}$  presents a higher correlation with  
511  $AOD_{AERONET}$  for shorter wavelengths, ranging  $r^2$  from 0.86 at 440 nm to 0.72 at 870 nm. In general, the  
512 AOD at 675 nm, and especially at 870 nm, presents more deviation between the data pairs than for the  
513 shorter wavelengths. Some outliers presenting high  $AOD_{GRASP\_ZEN}$  values can be appreciated, especially at  
514 shorter wavelengths; it could be caused by some spurious measurements likely contaminated by clouds that  
515 pass the cloud-screening criteria, or recorded with dirtiness, rain droplets or dust over the instrument (it  
516 must be frequently cleaned). AOD from GRASP-ZEN generally overestimates the AERONET values, as  
517 synthetic study of Section 4.2 points out, with median values of the differences of  $AOD_{GRASP\_ZEN}$  with  
518 respect to  $AOD_{AERONET}$  between 0.01 and 0.02 for all wavelengths; similar values appear for MBE, ranging  
519 from 0.01 to 0.03. The uncertainty in the retrieved  $AOD_{GRASP\_ZEN}$  is estimated by SD to be 0.03 for 440 and  
520 500 nm and 0.02 for 675 and 870 nm using as reference the values provided by AERONET.



## 521 5.2 Aerosol volume concentration

522 Regarding the total aerosol volume concentration, the retrieved values with GRASP-ZEN and the  
523 obtained from AERONET along the analysed period are shown in Figure 14. The time evolution shows  
524 generally a similar behaviour for both datasets with exception of some VCT extreme values more frequent  
525 in the GRASP-ZEN database. Here it can be also seen that for this parameter there is a higher temporal  
526 coverage from GRASP-ZEN than from AERONET. This is because unlike the AOD, which is obtained  
527 from direct irradiance measurements, usually carried out every 3 minutes, the aerosol volume concentration  
528 is obtained from AERONET inversion products, which are retrieved from the combination of AOD and  
529 sky radiance measurements. Sky radiances are performed less frequently than the direct sun ones, and  
530 inversions are only processed if the sky measurements are available and satisfy certain requirements  
531 (Sinyuk et al., 2020).

532 The VCT, VCC and VCC values from both datasets are shown in Figure 15 for the week from 16 to  
533 22 June 2020 (same days than Figure 12), showing again a similar behaviour for the two datasets. Figure  
534 15 also reveals that the GRASP-ZEN values are noisier and overestimates the AERONET values, especially  
535 for the fine mode.

536 In order to perform a quantitative analysis for the correlation between VCT, VCC and VCC from  
537 GRASP-ZEN and AERONET datasets a match-up has been done. In this case, the GRASP-ZEN values  
538 closest to the AERONET values within 5 minutes are chosen, obtaining a total of 4356 coincident points  
539 for each volume concentration. A higher temporal range is selected here because the inversion products are  
540 less frequent than AOD. In addition, we assume that these aerosol properties should not change significantly  
541 in 5 minutes.

542 The GRASP-ZEN volume concentrations are represented against the coincident AERONET ones in  
543 the density scatter plots of the upper panels of Figure 16 for fine, coarse and total values. Bottom panels of  
544 Figure 16 also show the frequency histograms of the differences between GRASP-ZEN and AERONET  
545 values of VCF, VCC and VCT. The best correlation is obtained for the total volume concentration with a  
546  $r^2$  about 0.66, while for fine and coarse volume concentration the determination coefficient is 0.57 and 0.56,  
547 respectively. Despite the lower correlation coefficients, the retrieved volume concentrations are rather  
548 precise with values of the median of the differences between GRASP-ZEN and AERONET datasets about  
549  $0.006$  and  $0.005 \mu\text{m}^3/\mu\text{m}^2$  for fine and coarse modes, respectively, and  $0.010 \mu\text{m}^3/\mu\text{m}^2$  for the VCT. The  
550 highest uncertainty on the retrieved volume concentrations is in the VCT, which presents a SD value about  
551  $0.20 \mu\text{m}^3/\mu\text{m}^2$ ; while for fine and coarse modes these values are  $0.009 \mu\text{m}^3/\mu\text{m}^2$  and  $0.016 \mu\text{m}^3/\mu\text{m}^2$ , which  
552 are close to the uncertainty offered by AERONET,  $0.01 \mu\text{m}^3/\mu\text{m}^2$ .

553 All of the results of this paper have been obtained using the GRASP-ZEN methodology based on the  
554 'models' approach, which is a suitable option for the current issue due to the reduced number of radiometric  
555 observations provided by the ZEN-R52. However, the versatility of GRASP code allows different strategies  
556 for the retrieval of aerosol properties. In this sense, we have considered other strategies in this study to  
557 choose the one which provides the best results. These strategies are based on the temporal multi-pixel  
558 approach offered by GRASP (Lopatin et al., 2021), that constraints the variation of aerosol properties in  
559 time, forcing them to vary smoothly. The multi-pixel approach was firstly used in combination with the  
560 'models' approach. In order to avoid the problems derived of having fixed aerosol models with fixed aerosol  
561 properties, the temporal multi-pixel was also used assuming the size distribution as a bimodal (fine and  
562 coarse modes) log-normal distribution and the refractive indices have no dependence on wavelength. None  
563 of the methods improved the retrieval of aerosol properties but slightly reduce it; likely due to the intrusion  
564 of contaminated measurements that influenced the retrieval, but they did reduce the computation time (the  
565 data of a full day are inverted all at the same time). Nevertheless, these strategies could be considered for  
566 future aerosol retrievals.

## 567 6. Conclusions

568 This paper has explored the capabilities to calibrate a ZEN-R52 radiometer using the GRASP  
569 (Generalized Retrieval of Atmosphere and Surface Properties) code and to retrieve aerosol properties from  
570 measured zenith sky radiances (ZSR) at four wavelengths. The ZSR values measured by the ZEN-R52  
571 radiometer for solar zenith angle (SZA) values below  $30^\circ$  are contaminated by stray sun light intramission  
572 and, hence, should not be used. For some latitudes this would result in the absence of measurements for



573 most of the time, and therefore a technical improvement in the instrument to correct this issue is  
574 recommended to the manufacturers.

575 The proposed methodology for the calibration of ZEN-R52, using simulated ZSR values has been  
576 contrasted, showing discrepancies lower than 6% respect to the calibration coefficients obtained against an  
577 integrating sphere. This proposed methodology incorporates the advantage that it includes the  
578 normalization used by GRASP and therefore there is not any need to use extraterrestrial spectra to normalize  
579 the data when they are used as input in GRASP.

580 A new inversion strategy, called GRASP-ZEN, has been proposed to retrieve aerosol properties with  
581 GRASP code using the ZSR values measured by ZEN-R52. An analysis with synthetic data has concluded  
582 that ZSR measurements are useful to derive aerosol optical depth (AOD), since these measurements are  
583 sensitive to aerosol load and type for the ZEN-R52 channels, at least for AOD at 440 nm below 1. This  
584 sensitivity decreases when SZA increases due to the decrease on the intensity of the ZSR values. A couple  
585 of tests with synthetic data have revealed that the GRASP-ZEN inversion strategy generally overestimates  
586 the AOD for all channels under real aerosol scenarios.

587 The GRASP-ZEN method has been applied to ZSR measurements recorded with a ZEN-R52  
588 radiometer at Valladolid (Spain) for two years and half. A direct comparison of some retrieved aerosol  
589 properties against independent AERONET (Aerosol Robotic Network) products has pointed out the  
590 accuracy and precision of the aerosol properties retrieved by GRASP-ZEN. The correlation between the  
591 AOD retrieved by GRASP-ZEN and AERONET is high, with determination coefficients ( $r^2$ ) about 0.86,  
592 0.85, 0.79 and 0.72 for 440, 500, 675 and 870 nm, respectively. The uncertainties on the retrieved AOD  
593 values are between  $\pm 0.02$  and  $\pm 0.03$  considering the AERONET values as reference. AERONET offers  
594 uncertainties about  $\pm 0.01$  for wavelengths above 440 nm, and therefore the uncertainty achieved by the  
595 proposed method is higher than the offered by the reference value.

596 With respect other aerosol properties, the GRASP-ZEN retrieval is limited for the intensive properties,  
597 like complex refractive index and some size distribution parameters due to the use of the 'models' approach  
598 of GRASP. Nevertheless, the retrieved volume concentrations, which are extensive properties, have been  
599 compared against the same independent AERONET products to quantify the relative accuracy and precision  
600 in these concentrations retrieved by GRASP-ZEN. The  $r^2$  obtained comparing the volume concentrations  
601 obtained with GRASP-ZEN with respect to the AERONET reference values show low values for the fine  
602 (0.57) and coarse (0.56) modes, while for the total volume concentration a higher value (0.66) has been  
603 obtained. Nevertheless, the median and standard deviation of the differences on volume concentration  
604 between GRASP-ZEN and AERONET are lower than  $0.01 \mu\text{m}^3/\mu\text{m}^2$  and  $0.02 \mu\text{m}^3/\mu\text{m}^2$ , respectively, for  
605 both fine and coarse mode and also total concentration. These results have indicated that GRASP-ZEN is  
606 capable to retrieve the aerosol volume concentrations with good accuracy and precision.

607 This paper shows the potential of a simple and robust radiometer like the ZEN-R52 as a possible  
608 alternative for aerosol properties retrieval in remote areas. The proposed methodology would require of a  
609 previous coincident period of measurements collocated with an AERONET CE318 photometer to achieve  
610 the calibration, and later could be deployed in a remote site in order to broaden the aerosol monitoring  
611 network. This paper also assesses the capability from GRASP to retrieve aerosol properties using only ZSR  
612 at 440, 500, 675 and 870 nm. The uncertainty and bias found in the retrieval show the limitations of the  
613 instrument and inversion strategy, but also demonstrate that the ZEN-R52, together with the developed  
614 GRASP-ZEN strategy, can provide useful information about the AOD and aerosol volume concentration  
615 for total, fine and coarse modes. This can be especially useful for remote areas or even in places with  
616 collocated a CE318 photometer in order to increase the time resolution.

617  
618



## 619 Acknowledgments

620 This research has been supported by the Ministerio de Ciencia e Innovación (grant no. PID2021-  
621 127588OB-I00), the Junta de Castilla y León (grant no. VA227P20). This publication is part of the  
622 TED2021-131211B-I00 project funded by MCIN/AEI/10.13039/501100011033 and European Union  
623 “NextGenerationEU”/PRTR. This article is based upon work from COST Action CA21119 HARMONIA,  
624 supported by COST (European Cooperation in Science and Technology) and has been supported by the  
625 European Metrology Program for Innovation and Research (EMPIR) within the joint research project  
626 EMPIR 19ENV04 MAPP. We especially thank the GOA-UVa staff members (Rogelio Carracedo, Patricia  
627 Martín-Sánchez and Javier Gatón), for helping with the research through the maintenance of the instruments  
628 and the station infrastructure.

## 629 References

- 630 Almansa, A. F., Cuevas, E., Barreto, Á., Torres, B., García, O. E., García, R. D., Velasco-Merino, C.,  
631 Cachorro, V. E., Berjón, A., Mallorquín, M., López, C., Ramos, R., Guirado-Fuentes, C., Negrillo,  
632 R., & de Frutos, Á. M. (2020). Column integrated water vapor and aerosol load characterization  
633 with the new ZEN-R52 radiometer. *Remote Sensing*, 12(9). <https://doi.org/10.3390/RS12091424>
- 634 Almansa, A. F., Cuevas, E., Torres, B., Barreto, Á., García, R. D., Cachorro, V. E., De Frutos, Á. M.,  
635 López, C., & Ramos, R. (2017). A new zenith-looking narrow-band radiometer-based system  
636 (ZEN) for dust aerosol optical depth monitoring. *Atmospheric Measurement Techniques*, 10(2),  
637 565–579. <https://doi.org/10.5194/AMT-10-565-2017>
- 638 Ångström, A. (1964). The parameters of atmospheric turbidity. *Tellus*, 16(1), 64–75.  
639 <https://doi.org/10.1111/J.2153-3490.1964.TB00144.X>
- 640 Barker, H. W., & Marshak, A. (2001). Inferring Optical Depth of Broken Clouds above Green Vegetation  
641 Using Surface Solar Radiometric Measurements. *Journal of the Atmospheric Sciences*, 58(20),  
642 2989–3006. [https://doi.org/10.1175/1520-0469\(2001\)058<2989:IODOBC>2.0.CO;2](https://doi.org/10.1175/1520-0469(2001)058<2989:IODOBC>2.0.CO;2)
- 643 Barreto, Á., Cuevas, E., Granados-Muñoz, M. J., Alados-Arboledas, L., Romero, P. M., Gröbner, J.,  
644 Kouremeti, N., Almansa, A. F., Stone, T., Toledano, C., Román, R., Sorokin, M., Holben, B.,  
645 Canini, M., & Yela, M. (2016). The new sun-sky-lunar Cimel CE318-T multiband photometer  
646 &ndash; A comprehensive performance evaluation. *Atmospheric Measurement Techniques*, 9(2),  
647 631–654. <https://doi.org/10.5194/AMT-9-631-2016>
- 648 Barreto, A., Román, R., Cuevas, E., Pérez-Ramírez, D., Berjón, A. J., Kouremeti, N., Kazadzis, S.,  
649 Gröbner, J., Mazzola, M., Toledano, C., Benavent-Oltra, J. A., Doppler, L., Juryšek, J., Almansa,  
650 A. F., Victori, S., Maupin, F., Guirado-Fuentes, C., González, R., Vitale, V., ... Yela, M. (2019).  
651 Evaluation of night-time aerosols measurements and lunar irradiance models in the frame of the  
652 first multi-instrument nocturnal intercomparison campaign. *Atmospheric Environment*, 202, 190–  
653 211. <https://doi.org/10.1016/J.ATMOSENV.2019.01.006>
- 654 Benavent-Oltra, J. A., Román, R., Andrés Casquero-Vera, J., Pérez-Ramírez, D., Lyamani, H., Ortiz-  
655 Amezcua, P., Bedoya-Velásquez, A. E., De Arruda Moreira, G., Barreto, Á., Lopatin, A., Fuentes,  
656 D., Herrera, M., Torres, B., Dubovik, O., Luis Guerrero-Rascado, J., Goloub, P., Olmo-Reyes, F. J.,  
657 & Alados-Arboledas, L. (2019). Different strategies to retrieve aerosol properties at night-time with  
658 the GRASP algorithm. *Atmospheric Chemistry and Physics*, 19(22), 14149–14171.  
659 <https://doi.org/10.5194/ACP-19-14149-2019>
- 660 Benavent-Oltra, J. A., Román, R., Granados-Munõz, M. J., Pérez-Ramírez, D., Ortiz-Amezcua, P.,  
661 Denjean, C., Lopatin, A., Lyamani, H., Torres, B., Guerrero-Rascado, J. L., Fuentes, D., Dubovik,  
662 O., Chaikovskiy, A., Olmo, F. J., Mallet, M., & Alados-Arboledas, L. (2017). Comparative  
663 assessment of GRASP algorithm for a dust event over Granada (Spain) during ChArMEx-  
664 ADRIMED 2013 campaign. *Atmospheric Measurement Techniques*, 10(11), 4439–4457.  
665 <https://doi.org/10.5194/AMT-10-4439-2017>
- 666 Bennouna, Y. S., Cachorro, V. E., Torres, B., Toledano, C., Berjón, A., de Frutos, A. M., & Alonso  
667 Fernández Coppel, I. (2013). Atmospheric turbidity determined by the annual cycle of the aerosol



- 668 optical depth over north-center Spain from ground (AERONET) and satellite (MODIS).  
669 *Atmospheric Environment*, 67, 352–364. <https://doi.org/10.1016/J.ATMOSENV.2012.10.065>
- 670 Boucher, O., Randall, D., Artaxo, P., Bretherton, C., Feingold, G., Forster, P., Kerminen, V., Kondo, Y.,  
671 Liao, H., Lohmann, U., Rasch, P., Satheesh, S., Sherwood, S., Stevens, B., & Zhang, X. (2013).  
672 Clouds and Aerosols. In: *Climate Change 2013: The Physical Science Basis. Contribution of*  
673 *Working Group I to the Fifth Assessment Report of the Intergovernmental Panel on Climate*  
674 *Change Coordinating Lead Authors: Lead Authors.*  
675 <https://doi.org/10.1017/CBO9781107415324.016>
- 676 Cachorro, V. E., Burgos, M. A., Mateos, D., Toledano, C., Bennouna, Y., Torres, B., De Frutos, Á. M., &  
677 Herguedas, Á. (2016). Inventory of African desert dust events in the north-central Iberian Peninsula  
678 in 2003-2014 based on sun-photometer-AERONET and particulate-mass-EMEP data. *Atmospheric*  
679 *Chemistry and Physics*, 16(13), 8227–8248. <https://doi.org/10.5194/ACP-16-8227-2016>
- 680 Chen, C., Dubovik, O., Fuertes, D., Litvinov, P., Lapyonok, T., Lopatin, A., Ducos, F., Derimian, Y.,  
681 Herman, M., Tanré, D., Remer, L. A., Lyapustin, A., Sayer, A. M., Levy, R. C., Christina Hsu, N.,  
682 Descloitres, J., Li, L., Torres, B., Karol, Y., ... Federspiel, C. (2020). Validation of GRASP  
683 algorithm product from POLDER/PARASOL data and assessment of multi-angular polarimetry  
684 potential for aerosol monitoring. *Earth System Science Data*, 12(4), 3573–3620.  
685 <https://doi.org/10.5194/ESSD-12-3573-2020>
- 686 Chiu, C. J., Huang, C.-H., Marshak, A., Slutsker, I., Giles, D. M., Holben, B. N., Knyazikhin, Y.,  
687 Wiscombe, W. J., Huang, C., Marshak, A., Slutsker, I., Giles, D. M., Holben, B. N., Knyazikhin,  
688 Y., & Wiscombe, W. J. (2010). Cloud optical depth retrievals from the Aerosol Robotic Network  
689 (AERONET) cloud mode observations. *Journal of Geophysical Research: Atmospheres*, 115(D14),  
690 14202. <https://doi.org/10.1029/2009JD013121>
- 691 Cissé, G., McLeman, R., Adams, H., Aldunce, P., Bowen, K., Campbell-Lendrum, D., Clayton, S., Ebi,  
692 K. L., Hess, J., Huang, C., Liu, Q., McGregor, G., Semenza, J., & Tirado, M. C. (2022). Health,  
693 Wellbeing, and the Changing Structure of Communities. In: *Climate Change 2022: Impacts,*  
694 *Adaptation, and Vulnerability. Contribution of Working Group II to the Sixth Assessment Report of*  
695 *the Intergovernmental Panel on Climate Change [H.-O. Pörtner, D.C. Roberts, M. Tignor, E.S.*  
696 *Poloczanska, K. Mintenbeck, A. Alegria, M. Craig, S. Langsdorf, S. Löschke, V. Möller, A. Okem,*  
697 *B. Rama (eds.)].* <https://doi.org/10.1017/9781009325844.008>.
- 698 Dubovik, O., Fuertes, D., Litvinov, P., Lopatin, A., Lapyonok, T., Dubovik, I., Xu, F., Ducos, F., Chen,  
699 C., Torres, B., Derimian, Y., Li, L., Herreras-Giralda, M., Herrera, M., Karol, Y., Matar, C.,  
700 Schuster, G. L., Espinosa, R., Puthukkudy, A., ... Federspiel, C. (2021). A Comprehensive  
701 Description of Multi-Term LSM for Applying Multiple a Priori Constraints in Problems of  
702 Atmospheric Remote Sensing: GRASP Algorithm, Concept, and Applications. *Frontiers in Remote*  
703 *Sensing*, 2, 23. <https://doi.org/10.3389/FRSEN.2021.706851>
- 704 Dubovik, O., & King, M. D. (2000). A flexible inversion algorithm for retrieval of aerosol optical  
705 properties from Sun and sky radiance measurements. *Journal of Geophysical Research:*  
706 *Atmospheres*, 105(D16), 20673–20696. <https://doi.org/10.1029/2000JD900282>
- 707 Dubovik, O., Lapyonok, T., Litvinov, P., Herman, M., Fuertes, D., Ducos, F., Torres, B., Derimian, Y.,  
708 Huang, X., Lopatin, A., Chaikovskiy, A., Aspöckl, M., & Federspiel, C. (2014). GRASP: a  
709 versatile algorithm for characterizing the atmosphere. *SPIE Newsroom*.  
710 <https://doi.org/10.1117/2.1201408.005558>
- 711 Eilers, P. H. C., & Goeman, J. J. (2004). Enhancing scatterplots with smoothed densities. *Bioinformatics*,  
712 20(5), 623–628. <https://doi.org/10.1093/BIOINFORMATICS/BTG454>
- 713 Espinosa, W. R., Remer, L. A., Dubovik, O., Ziemba, L., Beyersdorf, A., Orozco, D., Schuster, G.,  
714 Lapyonok, T., Fuertes, D., & Vanderlei Martins, J. (2017). Retrievals of aerosol optical and  
715 microphysical properties from Imaging Polar Nephelometer scattering measurements. *Atmospheric*  
716 *Measurement Techniques*, 10(3), 811–824. <https://doi.org/10.5194/AMT-10-811-2017>



- 717 Fuertes, D., Toledano, C., González, R., Berjón, A., Torres, B., Cachorro, V. E., & De Frutos, Á. M.  
718 (2018). CÆLIS: Software for assimilation, management and processing data of an atmospheric  
719 measurement network. *Geoscientific Instrumentation, Methods and Data Systems*, 7(1), 67–81.  
720 <https://doi.org/10.5194/GI-7-67-2018>
- 721 Giles, D. M., Sinyuk, A., Sorokin, M. G., Schafer, J. S., Smirnov, A., Slutsker, I., Eck, T. F., Holben, B.  
722 N., Lewis, J. R., Campbell, J. R., Welton, E. J., Korkin, S. V., & Lyapustin, A. I. (2019).  
723 Advancements in the Aerosol Robotic Network (AERONET) Version 3 database - Automated near-  
724 real-time quality control algorithm with improved cloud screening for Sun photometer aerosol  
725 optical depth (AOD) measurements. *Atmospheric Measurement Techniques*, 12(1), 169–209.  
726 <https://doi.org/10.5194/AMT-12-169-2019>
- 727 González, R., Toledano, C., Román, R., Fuertes, D., Berjón, A., Mateos, D., Guirado-Fuentes, C.,  
728 Velasco-Merino, C., Antuña-Sánchez, J. C., Calle, A., Cachorro, V. E., & De Frutos, Á. M. (2020).  
729 Daytime and nighttime aerosol optical depth implementation in CÆLIS. *Geoscientific  
730 Instrumentation, Methods and Data Systems*, 9(2), 417–433. <https://doi.org/10.5194/GI-9-417-2020>
- 731 Herreras, M., Román, R., Cazorla, A., Toledano, C., Lyamani, H., Torres, B., Cachorro, V. E., Olmo, F.  
732 J., Alados-Arboledas, L., & de Frutos, A. M. (2019). Evaluation of retrieved aerosol extinction  
733 profiles using as reference the aerosol optical depth differences between various heights.  
734 *Atmospheric Research*, 230, 104625. <https://doi.org/10.1016/J.ATMOSRES.2019.104625>
- 735 Herreras-Giralda, M., Litvinov, P., Dubovik, O., Derimian, Y., Lapyonok, T., Fuertes, D., Sourdeval, O.,  
736 Preusker, R., & Fischer, J. (2022). Thermal emission in the successive orders of scattering (SOS)  
737 radiative transfer approach. *Journal of Quantitative Spectroscopy and Radiative Transfer*, 291,  
738 108327. <https://doi.org/10.1016/J.JQSRT.2022.108327>
- 739 Holben, B. N., Eck, T. F., Slutsker, I., Tanré, D., Buis, J. P., Setzer, A., Vermote, E., Reagan, J. A.,  
740 Kaufman, Y. J., Nakajima, T., Lavenu, F., Jankowiak, I., & Smirnov, A. (1998). AERONET—A  
741 Federated Instrument Network and Data Archive for Aerosol Characterization. *Remote Sensing of  
742 Environment*, 66(1), 1–16. [https://doi.org/10.1016/S0034-4257\(98\)00031-5](https://doi.org/10.1016/S0034-4257(98)00031-5)
- 743 Lenoble, J., Herman, M., Deuzé, J. L., Lafrance, B., Santer, R., & Tanré, D. (2007). A successive order of  
744 scattering code for solving the vector equation of transfer in the earth's atmosphere with aerosols.  
745 *Journal of Quantitative Spectroscopy and Radiative Transfer*, 107(3), 479–507.  
746 <https://doi.org/10.1016/J.JQSRT.2007.03.010>
- 747 Lopatin, A., Dubovik, O., Chaikovskiy, A., Goloub, P., Lapyonok, T., Tanré, D., & Litvinov, P. (2013).  
748 Enhancement of aerosol characterization using synergy of lidar and sun-photometer coincident  
749 observations: The GARRLiC algorithm. *Atmospheric Measurement Techniques*, 6(8), 2065–2088.  
750 <https://doi.org/10.5194/AMT-6-2065-2013>
- 751 Lopatin, A., Dubovik, O., Fuertes, D., Stenchikov, G., Lapyonok, T., Veselovskii, I., Wienhold, F. G.,  
752 Shevchenko, I., Hu, Q., & Parajuli, S. (2021). Synergy processing of diverse ground-based remote  
753 sensing and in situ data using the GRASP algorithm: applications to radiometer, lidar and  
754 radiosonde observations. *Atmospheric Measurement Techniques*, 14(3), 2575–2614.  
755 <https://doi.org/10.5194/AMT-14-2575-2021>
- 756 Marshak, A., Knyazikhin, Y., Davis, A. B., Wiscombe, W. J., & Pilewskie, P. (2000). Cloud-vegetation  
757 interaction: Use of normalized difference cloud index for estimation of cloud optical thickness.  
758 *Geophysical Research Letters*, 27(12), 1695–1698. <https://doi.org/10.1029/1999GL010993>
- 759 Mateos, D., Cachorro, V. E., Velasco-Merino, C., O'Neill, N. T., Burgos, M. A., Gonzalez, R., Toledano,  
760 C., Herreras, M., Calle, A., & de Frutos, A. M. (2020). Comparison of three different  
761 methodologies for the identification of high atmospheric turbidity episodes. *Atmospheric Research*,  
762 237, 104835. <https://doi.org/10.1016/j.atmosres.2019.104835>
- 763 Molero, F., Pujadas, M., & Artñano, B. (2020). Study of the Effect of Aerosol Vertical Profile on  
764 Microphysical Properties Using GRASP Code with Sun/Sky Photometer and Multiwavelength



- 765 Lidar Measurements. *Remote Sensing* 2020, Vol. 12, Page 4072, 12(24), 4072.  
766 <https://doi.org/10.3390/RS12244072>
- 767 Myhre, G., Shindell, D., Bréon, F., Collins, W., Fuglestedt, J., Huang, J., Koch, D., Lamarque, J., Lee,  
768 D., Mendoza, B., Nakajima, T., Robock, A., Stephens, G., Takemura, T., & Zhang, H. (2013).  
769 Anthropogenic and Natural Radiative Forcing. In: *Climate Change 2013: The Physical Science*  
770 *Basis. Contribution of Working Group I.* <https://doi.org/10.1017/CBO9781107415324.018>
- 771 Nakajima, T., Tonna Glauco, Rao, R., Boi, P., Kaufman, Y., & Holben, B. (1996). Use of sky brightness  
772 measurements from ground for remote sensing of particulate polydispersions. *Applied Optics*, Vol.  
773 35, Issue 15, Pp. 2672-2686, 35(15), 2672–2686. <https://doi.org/10.1364/AO.35.002672>
- 774 Román, R., Antuña-Sánchez, J. C., Cachorro, V. E., Toledano, C., Torres, B., Mateos, D., Fuertes, D.,  
775 López, C., González, R., Lapyonok, T., Herreras-Giralda, M., Dubovik, O., & De Frutos, Á. M.  
776 (2022). Retrieval of aerosol properties using relative radiance measurements from an all-sky  
777 camera. *Atmospheric Measurement Techniques*, 15(2), 407–433. [https://doi.org/10.5194/AMT-15-](https://doi.org/10.5194/AMT-15-407-2022)  
778 [407-2022](https://doi.org/10.5194/AMT-15-407-2022)
- 779 Román, R., Benavent-Oltra, J. A., Casquero-Vera, J. A., Lopatin, A., Cazorla, A., Lyamani, H., Denjean,  
780 C., Fuertes, D., Pérez-Ramírez, D., Torres, B., Toledano, C., Dubovik, O., Cachorro, V. E., de  
781 Frutos, A. M., Olmo, F. J., & Alados-Arboledas, L. (2018). Retrieval of aerosol profiles combining  
782 sunphotometer and ceilometer measurements in GRASP code. *Atmospheric Research*, 204, 161–  
783 177. <https://doi.org/10.1016/J.ATMOSRES.2018.01.021>
- 784 Román, R., Bilbao, J., & de Miguel, A. (2014). Reconstruction of six decades of daily total solar  
785 shortwave irradiation in the Iberian Peninsula using sunshine duration records. *Atmospheric*  
786 *Environment*, 99, 41–50. <https://doi.org/10.1016/J.ATMOENV.2014.09.052>
- 787 Román, R., González, R., Toledano, C., Barreto, Á., Pérez-Ramírez, D., Benavent-Oltra, J. A., Olmo, F.  
788 J., Cachorro, V. E., Alados-Arboledas, L., & de Frutos, Á. M. (2020). Correction of a lunar-  
789 irradiance model for aerosol optical depth retrieval and comparison with a star photometer.  
790 *Atmospheric Measurement Techniques*, 13(11), 6293–6310. [https://doi.org/10.5194/AMT-13-6293-](https://doi.org/10.5194/AMT-13-6293-2020)  
791 [2020](https://doi.org/10.5194/AMT-13-6293-2020)
- 792 Román, R., Torres, B., Fuertes, D., Cachorro, V. E., Dubovik, O., Toledano, C., Cazorla, A., Barreto, A.,  
793 Bosch, J. L., Lapyonok, T., González, R., Goloub, P., Perrone, M. R., Olmo, F. J., de Frutos, A., &  
794 Alados-Arboledas, L. (2017). Remote sensing of lunar aureole with a sky camera: Adding  
795 information in the nocturnal retrieval of aerosol properties with GRASP code. *Remote Sensing of*  
796 *Environment*, 196, 238–252. <https://doi.org/10.1016/J.RSE.2017.05.013>
- 797 Schaaf, C., Liu, J., Gao, F., & Strahler, A. H. (2011). MODIS albedo and reflectance anisotropy products  
798 from Aqua and Terra, *Land Remote Sensing and Global Environmental Change: NASA's Earth*  
799 *Observing System and the Science of ASTER and MODIS*. 11, 549–561.
- 800 Sinyuk, A., Sinyuk, A., Holben, B. N., Eck, T. F., Eck, T. F., M. Giles, D., M. Giles, D., Slutsker, I.,  
801 Slutsker, I., Korkin, S., Korkin, S., S. Schafer, J., S. Schafer, J., Smirnov, A., Smirnov, A., Sorokin,  
802 M., Sorokin, M., & Lyapustin, A. (2020). The AERONET Version 3 aerosol retrieval algorithm,  
803 associated uncertainties and comparisons to Version 2. *Atmospheric Measurement Techniques*,  
804 13(6), 3375–3411. <https://doi.org/10.5194/AMT-13-3375-2020>
- 805 Titos, G., Ealo, M., Román, R., Cazorla, A., Sola, Y., Dubovik, O., Alastuey, A., & Pandolfi, M. (2019).  
806 Retrieval of aerosol properties from ceilometer and photometer measurements: Long-term  
807 evaluation with in situ data and statistical analysis at Montsec (southern Pyrenees). *Atmospheric*  
808 *Measurement Techniques*, 12(6), 3255–3267. <https://doi.org/10.5194/AMT-12-3255-2019>
- 809 Torres, B., Dubovik, O., Fuertes, D., Schuster, G., Eugenia Cachorro, V., Lapyonok, T., Goloub, P.,  
810 Blarel, L., Barreto, A., Mallet, M., Toledano, C., & Tanré, D. (2017). Advanced characterisation of  
811 aerosol size properties from measurements of spectral optical depth using the GRASP algorithm.  
812 *Atmospheric Measurement Techniques*, 10(10), 3743–3781. [https://doi.org/10.5194/AMT-10-3743-](https://doi.org/10.5194/AMT-10-3743-2017)  
813 [2017](https://doi.org/10.5194/AMT-10-3743-2017)





814 Tsekeri, A., Lopatin, A., Amiridis, V., Marinou, E., Igloffstein, J., Siomos, N., Solomos, S., Kokkalis, P.,  
 815 Engelmann, R., Baars, H., Gratsia, M., Raptis, P. I., Biniotoglou, I., Mihalopoulos, N., Kalivitis, N.,  
 816 Kouvarakis, G., Bartsotas, N., Kallos, G., Basart, S., ... Dubovik, O. (2017). GARRLiC and LIRIC:  
 817 strengths and limitations for the characterization of dust and marine particles along with their  
 818 mixtures. *Atmospheric Measurement Techniques*, 10(12), 4995–5016.  
 819 <https://doi.org/10.5194/AMT-10-4995-2017>

820 Walker, J. H., Cromer, C. L., & McLean, J. T. (1991). Calibration of passive remote observing optical  
 821 and microwave instrumentation. *Proc. SPIE—The International Soc. of Optical Engineering*, 3–5  
 822 April, Orlando, FL, 1493, 224–230.

823 Wei, Y., Li, Z., Zhang, Y., Chen, C., Xie, Y., Lv, Y., & Dubovik, O. (2021). Derivation of PM10 mass  
 824 concentration from advanced satellite retrieval products based on a semi-empirical physical  
 825 approach. *Remote Sensing of Environment*, 256, 112319.  
 826 <https://doi.org/10.1016/J.RSE.2021.112319>

827

828 **List of Tables**

829 **Table 1.** Calibration coefficients obtained using simulations of zenith sky radiance (Coef-SIM) and the  
 830 ones obtained at the IARC against a calibrated integrating sphere (Coef-IARC). The relative difference ( $\Delta$ )  
 831 between both coefficients is included assuming Coef-IARC as reference.

$\lambda$ (nm)	Coef – SIM ( $W/m^2nmsr$ )	Coef- IARC ( $W/m^2nmsr$ )	$\Delta$ (%)
440	3.2928e-05	3.2485e-05	1.39
500	1.1426e-05	1.2223e-05	-6.54
675	2.0734e-05	2.2221e-05	-6.72
870	1.6840e-05	1.7901e-05	-5.89

832

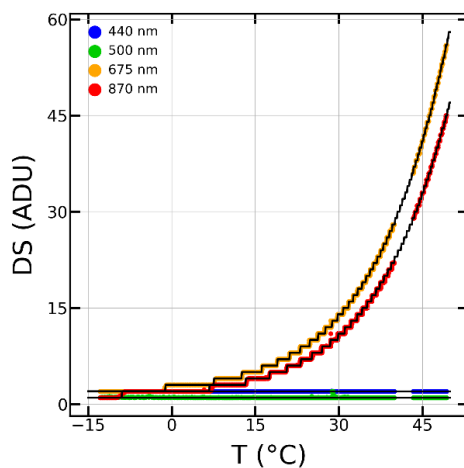
833 **Table 2.** Determination coefficient ( $r^2$ ) between ZSR<sub>ZEN</sub> and ZSR<sub>PPL</sub> and the mean (MBE), median (Md)  
 834 and standard deviation (SD) of the  $\Delta$  differences between ZSR<sub>ZEN</sub> and ZSR<sub>PPL</sub> at 440nm, 500nm, 675 nm  
 835 and 870 nm using the calibration coefficient obtained in this paper with simulated ZSR values and the ones  
 836 obtained with an integrating sphere at IARC in parenthesis. N represents the number of coincident ZSR<sub>ZEN</sub>  
 837 and ZSR<sub>PPL</sub> data pairs.

	$\lambda$ (nm)	$r^2$	MBE (%)	SD (%)	Md (%)	N
This paper (IARC)	440	0.99	1.96	3.00	1.36	1327
		(0.99)	(0.73)	(2.95)	(0.16)	
	500	0.99	-0.34	4.62	-1.39	1317
		(0.99)	(6.67)	(4.95)	(5.56)	
	675	0.95	3.76	12.54	-0.22	1289
		(0.95)	(14.67)	(13.92)	(10.96)	
	870	0.94	10.56	21.37	4.99	1165
		(0.94)	(26.67)	(25.13)	(20.96)	

838

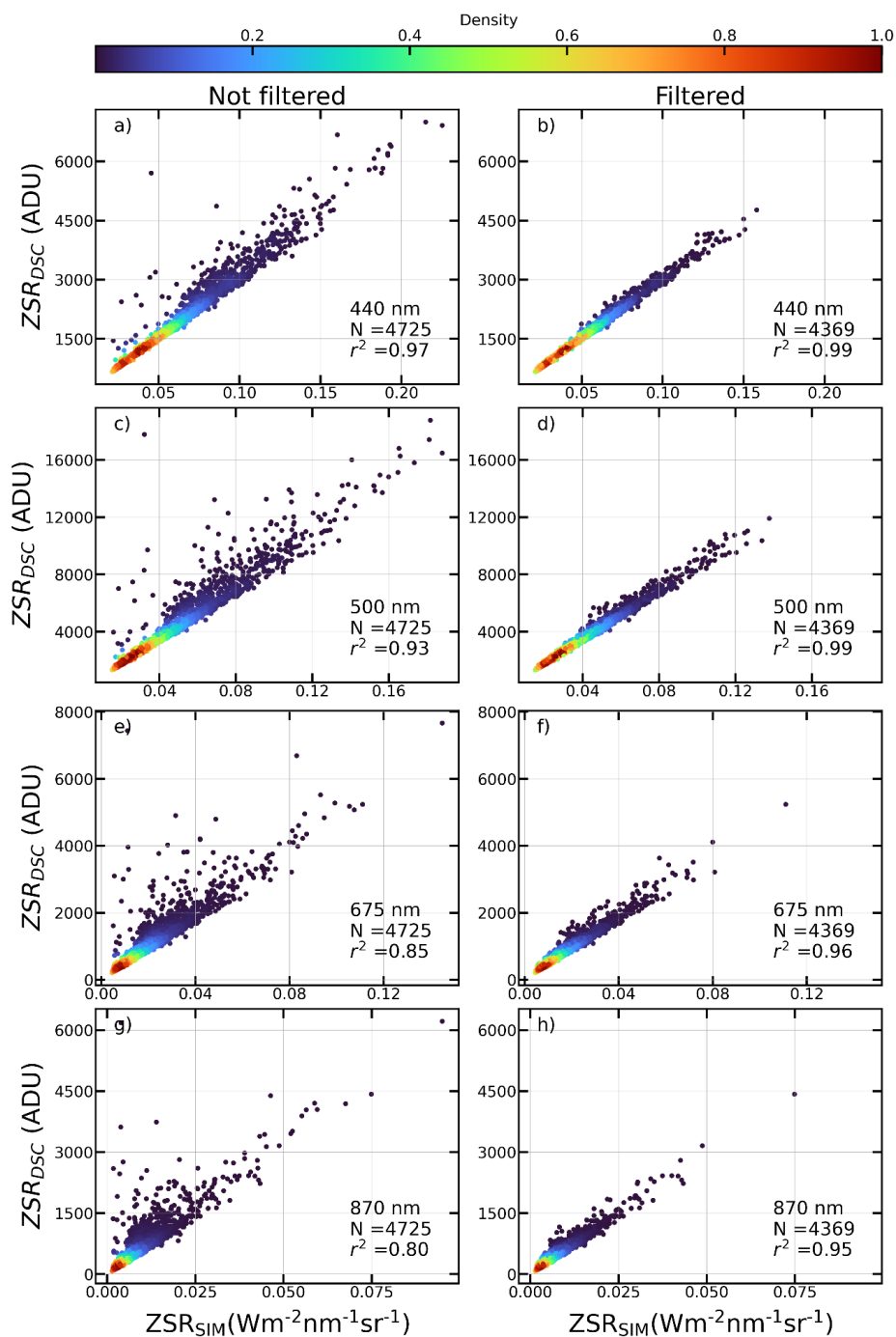
839

840 **List of Figures**



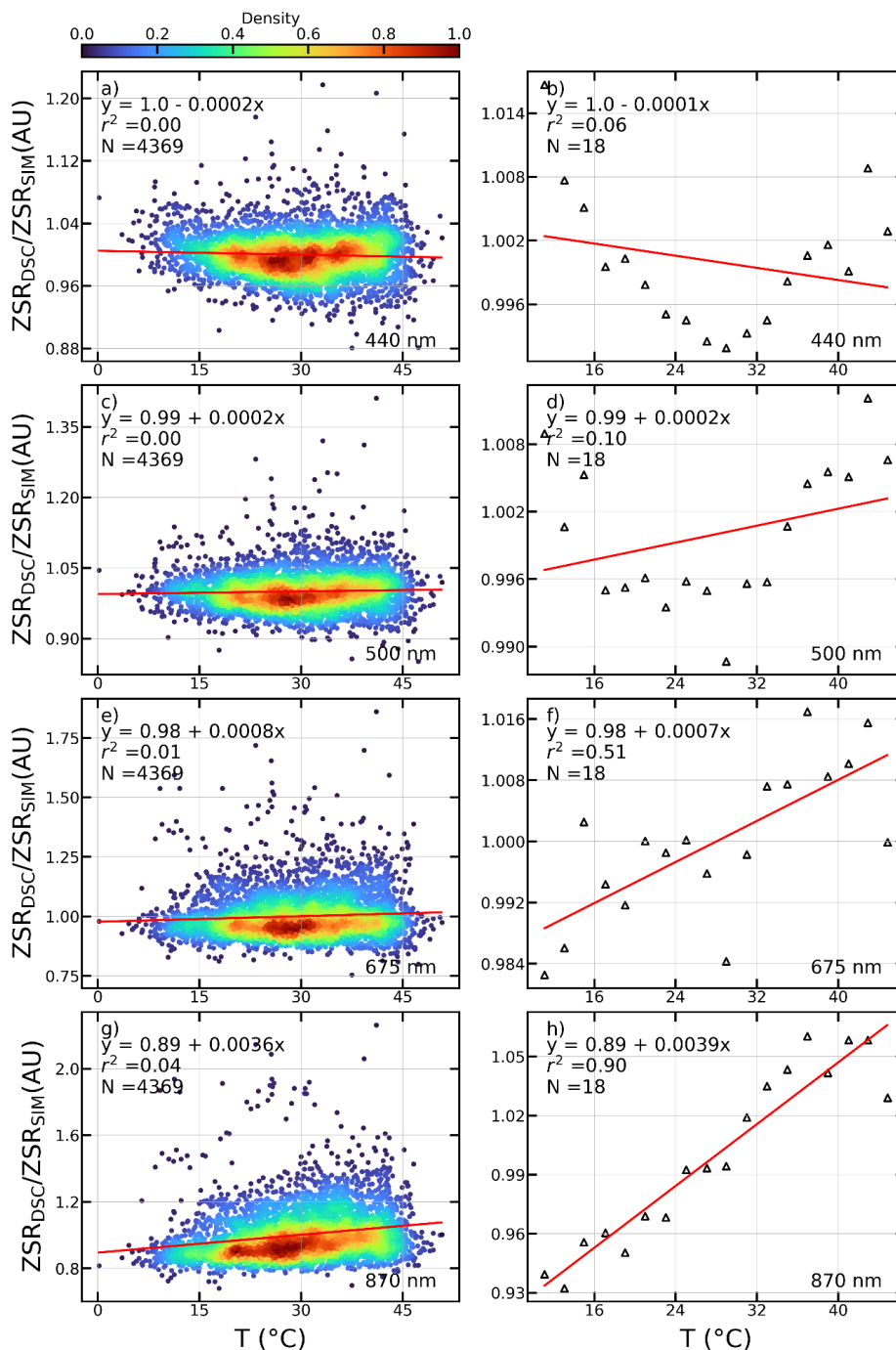
841  
842  
843  
844

Figure 1. ZEN-R52 dark signal (DS) in analogic-to-digital units (ADU) against the temperature (coloured dots) at 440, 500, 675 and 870 nm. Black lines represent the DS for each channel.



845  
846  
847  
848  
849  
850

Figure 2. Density scatter plot of the measured zenith sky radiances corrected from dark signal ( $ZSR_{DSC}$ ), in analogic-to-digital units (ADU), against the zenith sky radiances simulated by GRASP ( $ZSR_{SIM}$ ), both at 440 nm (upper panels), 500 nm (second row panels), 675 nm (third row panels) and 870 nm (bottom panels). Left and right panels show these data before and after applying a quality control filtering, respectively. Determination coefficient ( $r^2$ ) and number of data pairs (N) are also shown.



851

852

853 **Figure 3.** Left panel. density scatter plots for the normalized ratios  $ZSR_{DSC}/ZSR_{SIM}$  in arbitrary units (AU)

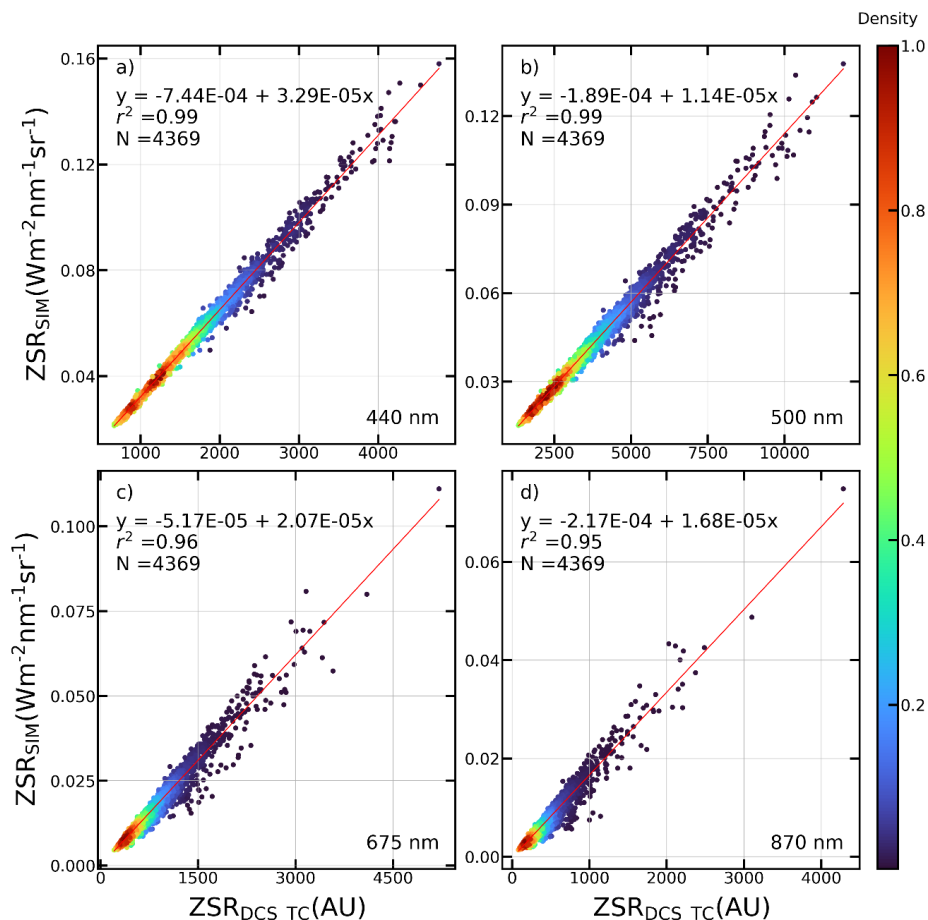
854 against the temperature at a) 440nm, c) 500nm, e) 675 nm and g) 870 nm. Right panel. scatter plot of the median

855 value for the ratios  $ZSR_{DSC}/ZSR_{SIM}$  grouped in 2°C ranges against mean temperature of the group at b) 440nm,



856 d) 500nm, f) 675 nm and h) 870 nm. Linear fit (red line), determination coefficient ( $r^2$ ) and its equation and  
857 number of data points (N) are also shown.

858



859

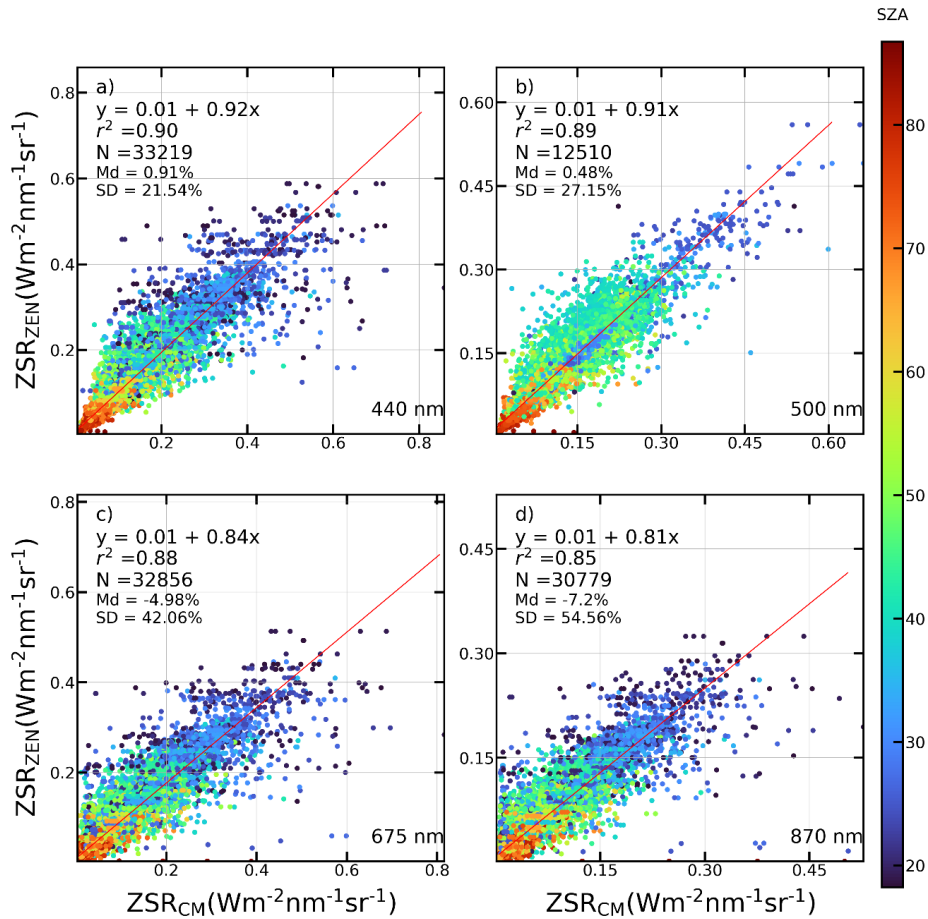
860

861 Figure 4. Density scatter plot of the zenith sky radiance simulated ( $ZSR_{SIM}$ ) in radiance units against the ZEN-

862 R52 measurements in arbitrary units (AU) corrected in dark signal and temperature ( $ZSR_{DCS\_TC}$ ) at a) 440nm,

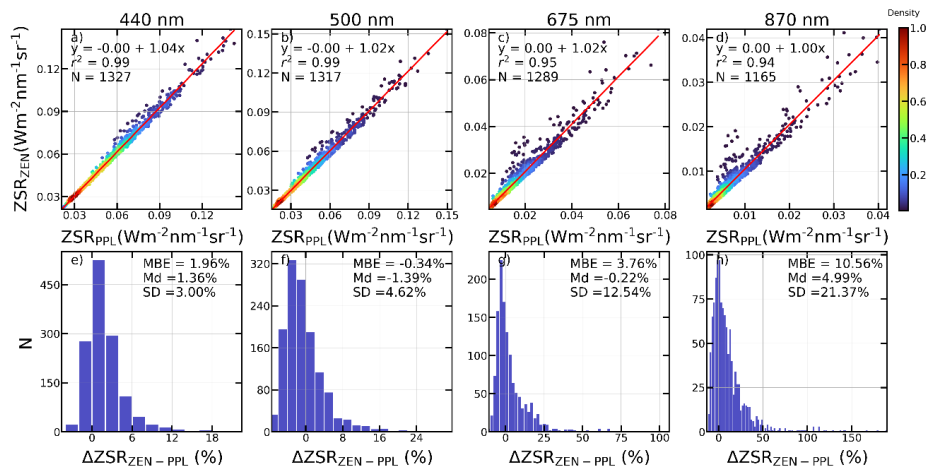
863 b) 500nm, c) 675 nm and d) 870 nm. Linear fit (red line) and its equation, determination coefficient ( $r^2$ ) and

number of data points (N) are also shown.



864  
865  
866  
867  
868

Figure 5. Scatter plot of the calibrated ZEN measurements ( $ZSR_{ZEN}$ ) against coincident measurements from AERONET Cloud Mode ( $ZSR_{CM}$ ) at a) 440nm, b) 500nm, c) 675 nm and d) 870 nm. Linear fit (red line) and its equation, determination coefficient ( $r^2$ ) and number of data points ( $N$ ) are shown. The median ( $Md$ ) and standard deviation ( $SD$ ) of the  $\Delta$  differences are also shown. Points colours represent the SZA.



869



870

871

872

873

874

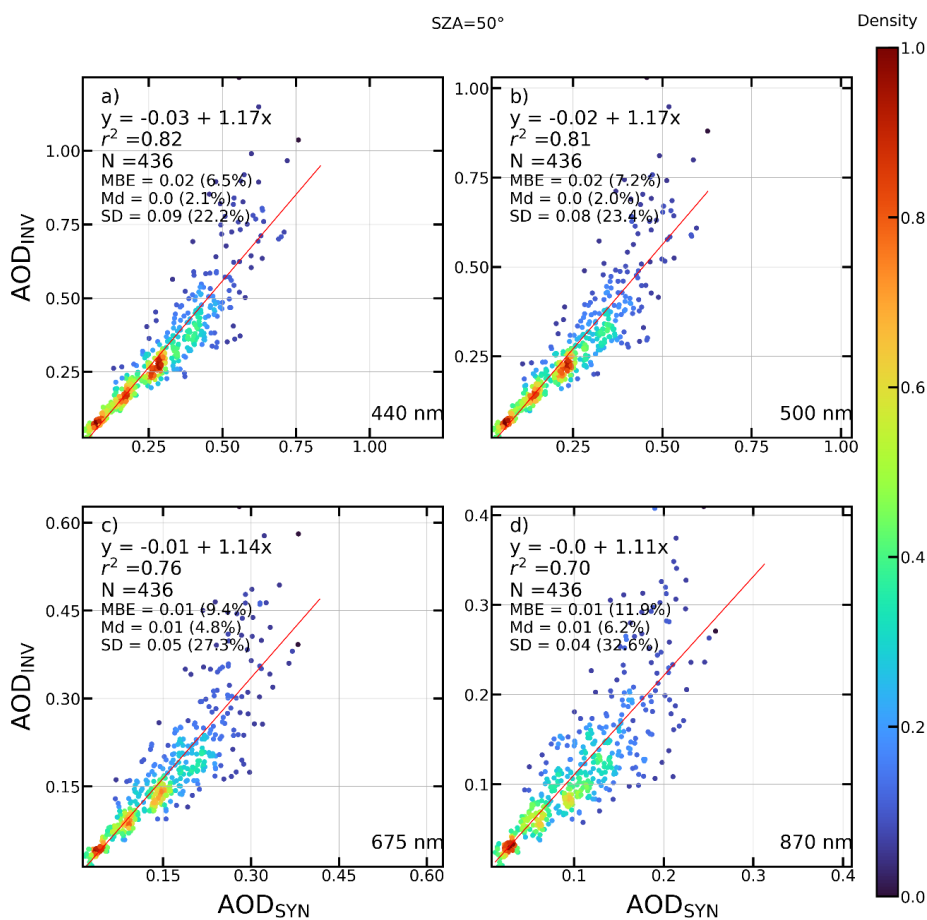
875

876

877

878

Figure 6. (a-d) Density scatter plot of the calibrated ZEN-R52 measurements ( $ZSR_{ZEN}$ ) against coincident zenith sky radiances derived from AERONET PPL measurements ( $ZSR_{ZEN-PPL}$ ) at a) 440 nm, b) 500 nm, c) 675 nm and d) 870 nm. Linear fit (red line), its equation, determination coefficient ( $r^2$ ) and number of data pairs (N) are shown. (e-h) Frequency histograms of the  $\Delta ZSR_{ZEN-PPL}$  differences in AOD from ZEN-R52 and AERONET PPL e) 440 nm, f) 500 nm, g) 675 nm and h) 870 nm. The mean bias error (MBE), median (Md) and standard deviation (SD) of the differences are also shown.



879

880

881

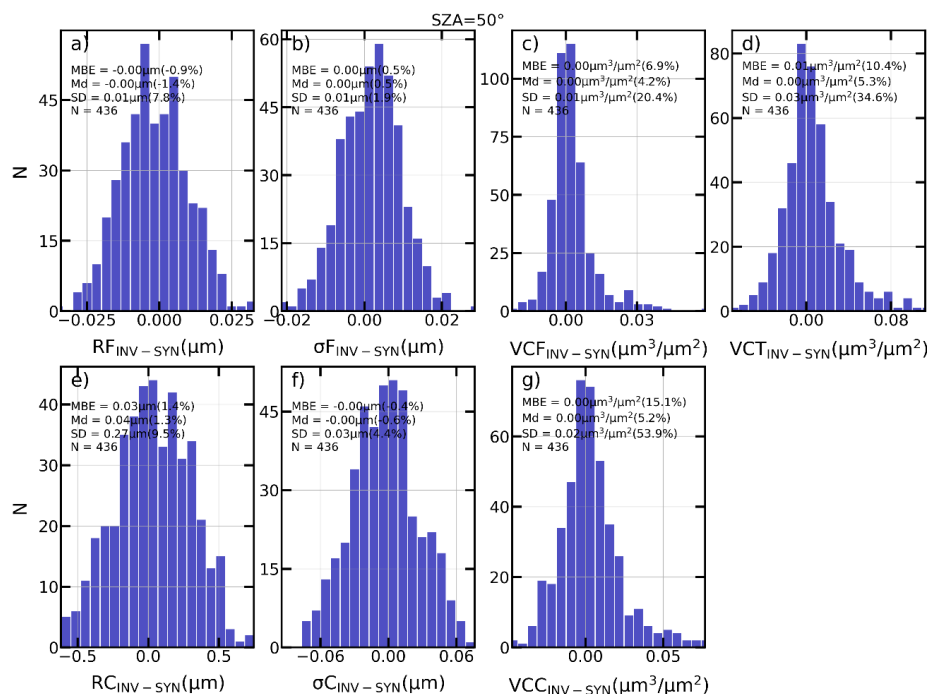
882

883

884

885

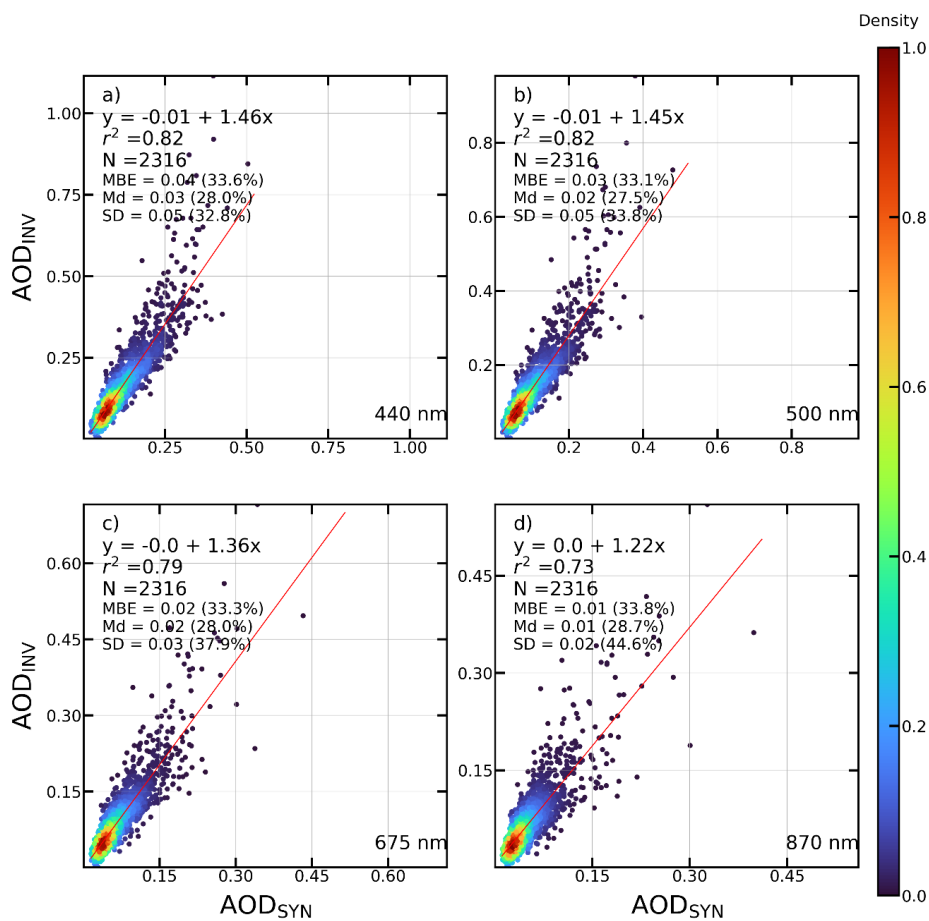
Figure 7. Density scatter plot of the AOD retrieved by GRASP after the inversion of synthetic ZSR ( $AOD_{INV}$ ) against the initial AOD ( $AOD_{SYN}$ ) obtained for synthetic scenarios created from the combination of five aerosol types for SZA=50° at a) 440nm, b) 500nm, c) 675 nm and d) 870 nm. Linear fit (red line) with its equation, determination coefficient ( $r^2$ ) and number of data points (N) are shown. Mean bias error (MB), median (Md) and standard deviation (SD) of the absolute and  $\Delta$  (between brackets) differences between the inverted and synthetic AOD are also included.



886  
887  
888  
889  
890  
891  
892  
893

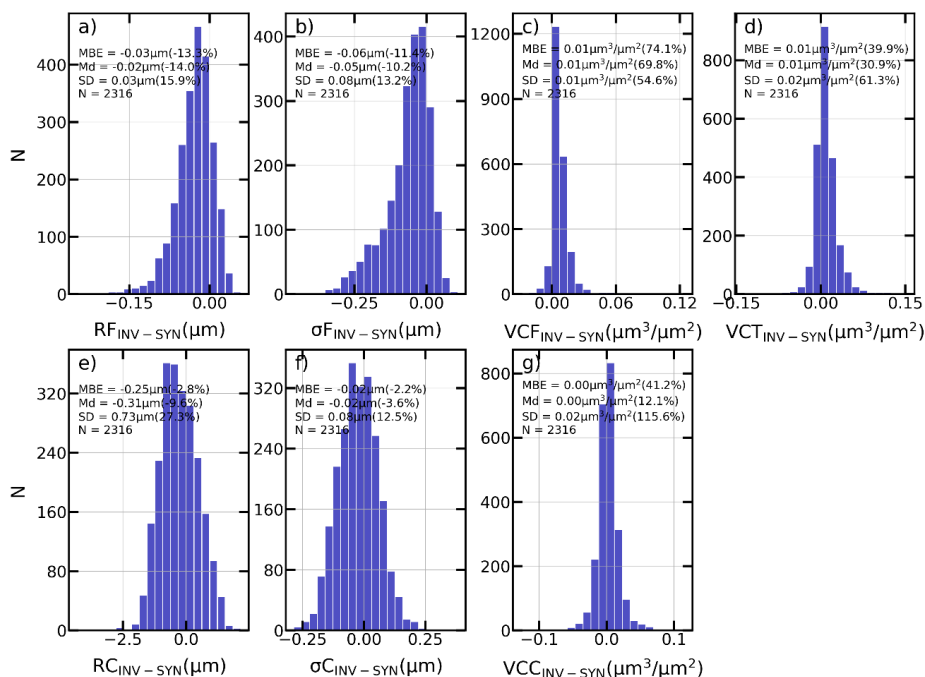
**Figure 8.** Frequency histograms of the absolute differences in the aerosol size distribution properties retrieved by GRASP after the inversion of synthetic ZSR (INV) and the ones initially obtained (SYN) for synthetic scenarios created from the combination of five aerosol types at SZA=50°. The mean bias error (MBE), median (Md) and standard deviation (SD) and their corresponding value for the  $\Delta$  differences (between brackets) are also shown. These size distribution properties are volume median radius of fine (RF) and coarse (RC) modes, standard deviation of log-normal distribution for fine ( $\sigma F$ ) and coarse modes ( $\sigma C$ ), and aerosol volume concentration for fine (VCF) and coarse (VCC) modes and the total (VCT).





894

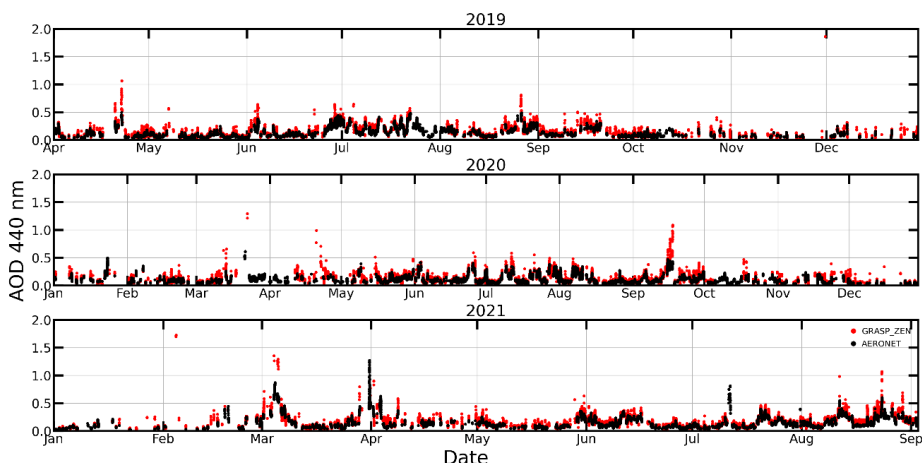
895 **Figure 9.** Density scatter plot of the AOD retrieved by GRASP after the inversion of synthetic ZSR ( $AOD_{INV}$ )  
 896 against the initial AOD ( $AOD_{SYN}$ ) obtained for synthetic scenarios created from AERONET retrievals at a)  
 897 440nm, b) 500nm, c) 675 nm and d) 870 nm. Linear fit (red line) with its equation, determination coefficient ( $r^2$ )  
 898 and number of data points ( $N$ ) are shown. Mean bias error (MB), median (Md) and standard deviation (SD) of  
 899 the absolute and  $\Delta$  (between brackets) differences between the inverted and synthetic AOD are also included.



900

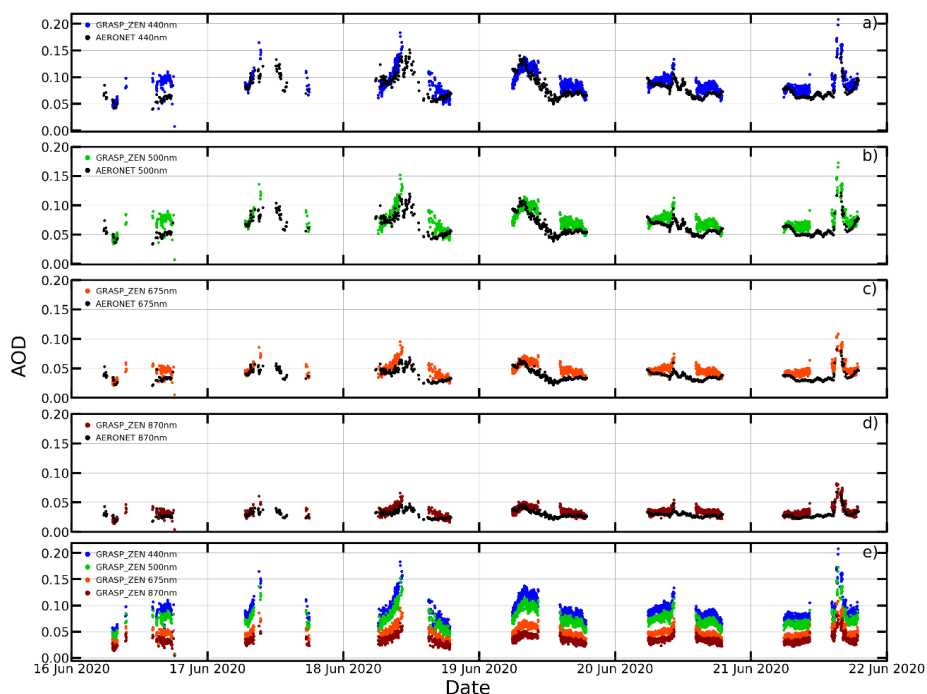
901 **Figure 10.** Frequency histograms of the absolute differences in the aerosol size distribution properties retrieved  
 902 by GRASP after the inversion of synthetic ZSR (INV) and the ones initially obtained (SYN) for synthetic  
 903 scenarios created from AERONET retrievals. The mean bias error (MBE), median (Md) and standard deviation  
 904 (SD) and their corresponding value for the  $\Delta$  differences (between brackets) are also shown. These size  
 905 distribution properties are volume median radius of fine (RF) and coarse (RC) modes, standard deviation  
 906 of log-normal distribution for fine ( $\sigma F$ ) and coarse modes ( $\sigma C$ ), and aerosol volume concentration for fine (VCF)  
 907 and coarse (VCC) modes and the total (VCT).

908

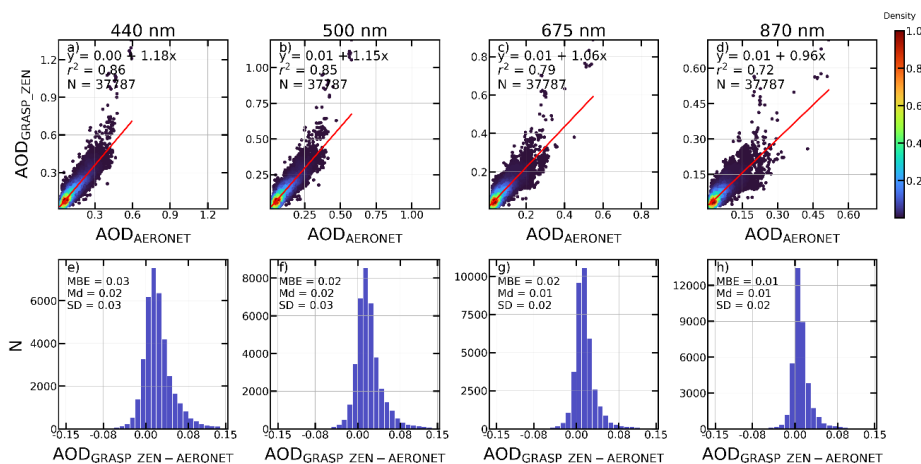


909

910 **Figure 11.** Time series evolution of aerosol optical depth (AOD) at 440 nm retrieved by GRASP-ZEN and by  
 911 AERONET at Valladolid for all the ZEN-R52 available dataset (April 2019 to September 2021).

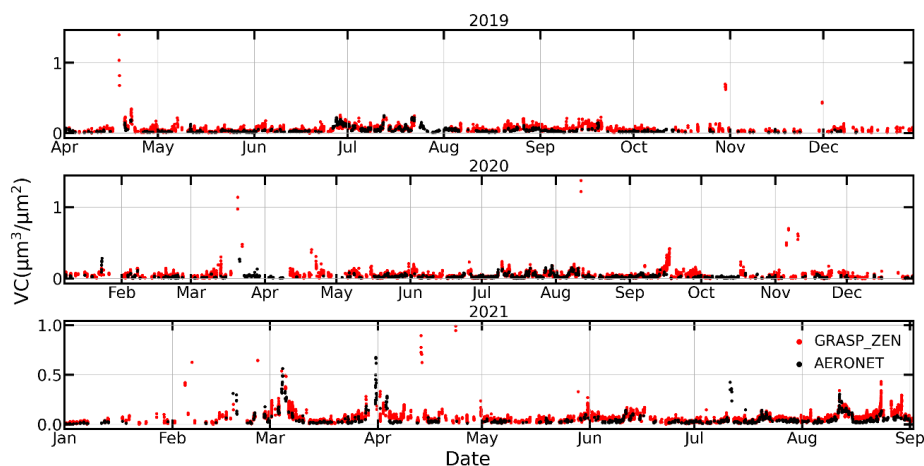


912  
913 **Figure 12.** (a-d) Time series evolution of aerosol optical depth (AOD) at a) 440 nm, b) 500 nm, c) 675 nm and d)  
914 870 nm retrieved by GRASP-ZEN and by AERONET at Valladolid for a week period in summer 2020 (16 to 22  
915 June). (e) AOD retrieved by GRASP-ZEN for all ZEN-R52 channels plotted together.



916  
917 **Figure 13.** (a-d) Density scatter plots of the AOD retrieved by GRASP-ZEN ( $AOD_{GRASP\_ZEN}$ ) against coincident  
918 measurement from AERONET ( $AOD_{AERONET}$ ) at a) 440 nm, b) 500 nm, c) 675 nm and d) 870 nm. Linear fit (red  
919 line), its equation, determination coefficient ( $r^2$ ) and number of data pairs (N) are shown. (e-h) Frequency  
920 histograms of the absolute differences in AOD from GRASP-ZEN and AERONET at e) 440nm, f) 500nm, g) 675  
921 nm and h) 870 nm. The mean bias error (MBE), median (Md) and standard deviation (SD) are also shown.

922

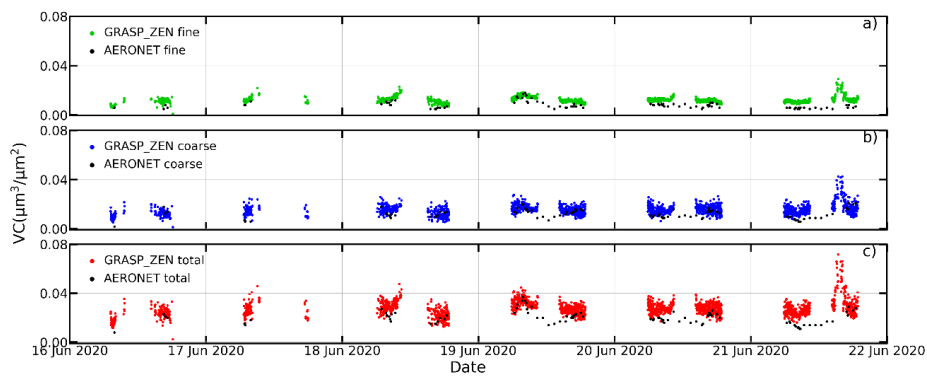


923

924

925

**Figure 14.** Time series evolution of the total volume concentration (VCT) retrieved by GRASP-ZEN and by AERONET at Valladolid for all the ZEN-R52 available dataset (April 2019 to September 2021).



926

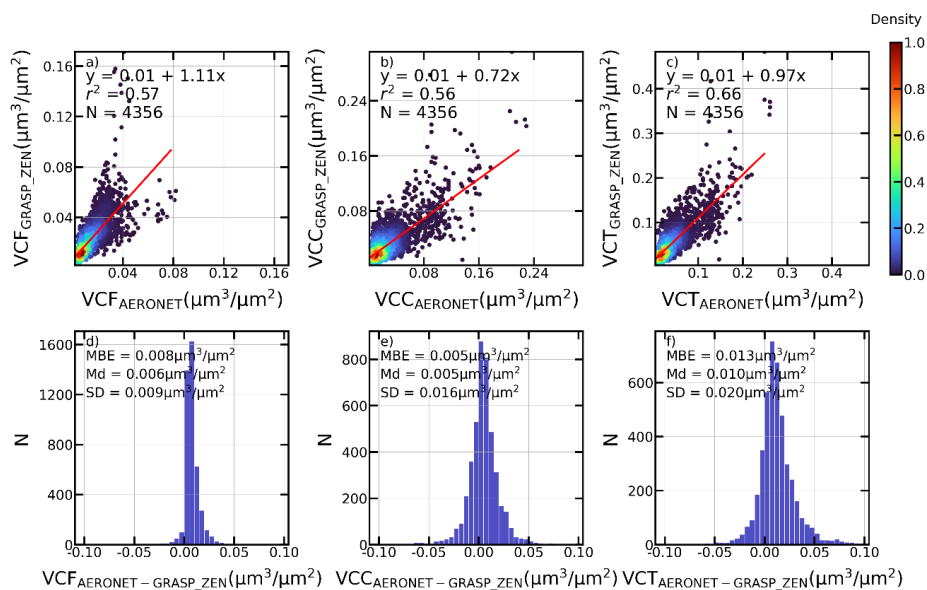
927

928

929

930

**Figure 15.** Time series evolution of volume concentration for fine (VCF) and coarse (VCC) modes and the total (VCT) retrieved by GRASP-ZEN and by AERONET at Valladolid for a week period in summer 2020 (16 to 22 June).



931  
 932 **Figure 16.** (a-c) Density scatter plot of the volume concentration for fine (VCF) and coarse (VCC) modes and  
 933 total (VCT) retrieved by GRASP-ZEN against coincident retrievals from AERONET. Linear fit (red line), its  
 934 equation, determination coefficient ( $r^2$ ) and number of data points (N) are shown. (e-h) Frequency histograms  
 935 of the absolute differences between both datasets. The mean bias error (MBE), median (Md) and standard  
 936 deviation (SD) are also shown.